Geoderma 284 (2016) 57–72

Contents lists available at ScienceDirect

Geoderma

journal homepage: www.elsevier.com/locate/geoderma

Rates and geochemical processes of soil and salt crust formation in Salars of the Atacama Desert, Chile

Kari Finstad [a,*], Marco Pfeiffer [a,b], Gavin McNicol [a,c], Jaime Barnes [d], Cecilia Demergasso [e], Guillermo Chong [f], Ronald Amundson [a]

[a] Department of Environmental Science, Policy and Management, University of California, Berkeley, 137 Mulford Hall, Berkeley, CA 94720, USA
[b] Departamento de Ingeniería y Suelos, Facultad de Ciencias Agronómicas, Universidad de Chile, Santa Rosa 11315, La Pintana, Chile
[c] Center for Accelerator Mass Spectrometry, Lawrence Livermore National Laboratory, Livermore, CA 94550, USA
[d] Department of Geological Sciences, University of Texas, Austin, TX 78712, USA
[e] Centro de Biotecnología, Universidad Católica del Norte, Antofagasta, Chile
[f] Departamento de Ciencias Geológicas, Universidad Católica del Norte, Antofagasta, Chile

ARTICLE INFO

Article history:
Received 3 May 2016
Received in revised form 25 August 2016
Accepted 28 August 2016
Available online xxxx

Keywords:
Groundwater
Salts
Evaporation
Isotope
Salt crust

ABSTRACT

The hyperarid Atacama Desert contains numerous local basins with surficial salt crusts, known as salars, where evaporation of shallow groundwater drives the major soil processes. We examine chemical and isotopic profiles in two soils of differing ages from the Salar Llamara to determine the geochemical processes involved in their formation. Evaporation, which provides salts to the soils through mineral precipitation, decreases with increasing salt crust thickness, and average ~ 0.03 mm m^{-2} d^{-1} over geological time frames. Salt distribution varies predictably with depth and soil age, with the most soluble compounds concentrated nearest to the land surface, indicating the direction of fluid flow. $\delta^{34}S$ values of mineral sulfate tend to decrease with decreasing soil depth, following a pattern indicative of Rayleigh-like fractionation as solute-rich waters migrate toward the land surface. $\delta^{13}C$ and $\delta^{18}O$ values of carbonate suggest that the uppermost halite layers, which contain very small amounts of carbonate, have a strong biological signature. In contrast, carbonate-rich layers deeper in the profiles consist of largely unmodified lacustrine carbonate that formed in highly evaporitic lake conditions. The continuous upward evaporation of water and dissolved solutes creates a rugged and physically dynamic halite crust composed of rounded salt nodules. The crust undergoes deliquescence as atmospheric relative humidity rises from marine air intrusions, and we found that the halite nodules on the surface of the Salar Llamara are nearly always at or above deliquescence relative humidity. The interiors of these nodules are therefore able to buffer the large diurnal changes in atmospheric relative humidity allowing for the survival of halophilic microbial communities in an otherwise very dry environment. Radiocarbon measurements of occluded organic C in the surface crusts indicate that C cycling occurs at differing rates depending on local micrometeorological conditions, and that a given salt crust feature may persist for thousands of years once formed.

1. Introduction

Geochemical processes in the Atacama Desert are limited by water. Most of the region consists of uplands and alluvial fans dependent on sparse rainfall (<2 mm y^{-1}) to drive soil and geochemical processes. However, the region also contains closed basins that receive both surface runoff and subsurface flow from the adjacent High Andes. Once a lake or wetland is desiccated, the evaporation of shallow groundwater by capillary flow promotes an upward movement of solutes, a direction that is the reverse of the normal water trajectory of most desert soils (Finstad et al., 2014). Studies of soil formation in these geological settings are very limited, and none have been conducted in northern Chile.

In Chile, salt covered evaporitic basins are called salars and are distinguishable by the hard salt crusts commonly found on their surfaces (Chong, 1984; Ericksen and Salas, 1990). Approximately half of the salars in northern Chile contain halite (NaCl) crusts, an area of >4000 km^2 (Stoertz and Ericksen, 1974). Most of the salars are located in the Andes, with only a handful in the Central Depression near to the Pacific coast. Salars in this region of the world are of growing significance. First, they contribute to an understanding of climate and hydrologic change, providing insight into both regional environmental changes and patterns of occupation by early hunter-gatherers and agriculturalists (Latorre et al., 2013). Second, fluid migration and chemical fractionation have locally deposited economically viable concentrations of iodine, boron, and other salts (Boschetti et al., 2007; Perez-Fodich et al., 2014; Chong et al., 2000). Finally, and somewhat paradoxically, salt crusts on the surface of salars can

* Corresponding author.
E-mail address: karifinstad@berkeley.edu (K. Finstad).

http://dx.doi.org/10.1016/j.geoderma.2016.08.020
0016-7061/

harbor microbial communities persisting on liquid water obtained through the deliquescence of halite (Davila et al., 2013). Presently, there is only a preliminary understanding of the geological evolution of these crusts and on how these processes influence the microbial communities (Artieda et al., 2015).

A pedogenic process-oriented understanding of salar evolution is still lacking. The objectives of this paper are twofold. First, we wished to characterize the resulting chemical nature and properties of the soils from the continuous evaporation of shallow groundwater and calculate rates of long-term water evaporation and salt accumulation. Second, we hoped to develop a conceptual model of surface halite crust formation and assess the capacity of this unique environment to support microbial life. We focused on two sites in the Salar Llamara, one 15,484 cal yr BP and one 19,348 cal yr BP, to examine the chemical and isotopic evolution of these soils at different time steps, with the goal of monitoring the soil environment to provide constraints to process-based models of water and salt movement.

2. Geological setting

The Salar Llamara lies in the Central Depression in northern Chile (Figs. 1 and 2). Since the Miocene the area has been part of an evaporitic basin, one which developed an outlet to the Pacific Ocean sometime in the late Pliocene or early Pleistocene (Pueyo et al., 2001; Saez et al., 1999). In the more recent geological past, the area of evaporite deposits is constrained to an area of approximately 205 km^2. Lakes or wetlands were likely formed during episodes of increased Andean runoff (Gayo et al., 2012; Nester et al., 2007; Rech et al., 2002), and their subsequent drying has formed distinctive salar characteristics. The surface is primarily covered with a dense, rugged salt crust composed of sodium chloride. Rounded features, referred to as salt nodules, are common features of Coastal Range and Central Valley salars, developing from the slow recrystallization of salt on the surface in the absence of precipitation (Stoertz and Ericksen, 1974), influenced by the presence of fog.

One site is located on a young unit of lacustrine origin, mapped as PlHs (undifferentiated Pleistocene-Holocene saline deposits of halite, sulfate, and nitrates). The other site is slightly higher in elevation and is either lacustrine in origin or formed on the distal end of an alluvial fan, and is mapped as PlHa(p) (Pleistocene-Holocene alluvial deposits of antiquity, playa facies) (Quezada et al., 2012) (Fig. 3). For simplicity, we refer to them here as Qh and Qp, respectively. Underlying the halite crust in both locations is a very fine-grained, laminated sediment consistent with a lacustrine or distal alluvial fan depositional environment. Occasional strata of what appear to be freshwater marls are also present in the Qh profile, which indicate the past occurrence of standing water

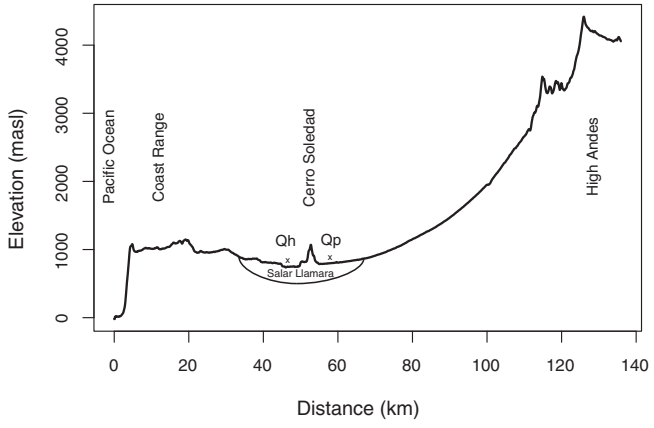

Fig. 1. Elevation profile of the Salar Llamara and field sites. The Salar Llamara sits in the Central Depression created by the High Andes to the east and Coast Range to the west. Digital elevation model (DEM) was taken from GeoMapApp (www.geomapapp.org).

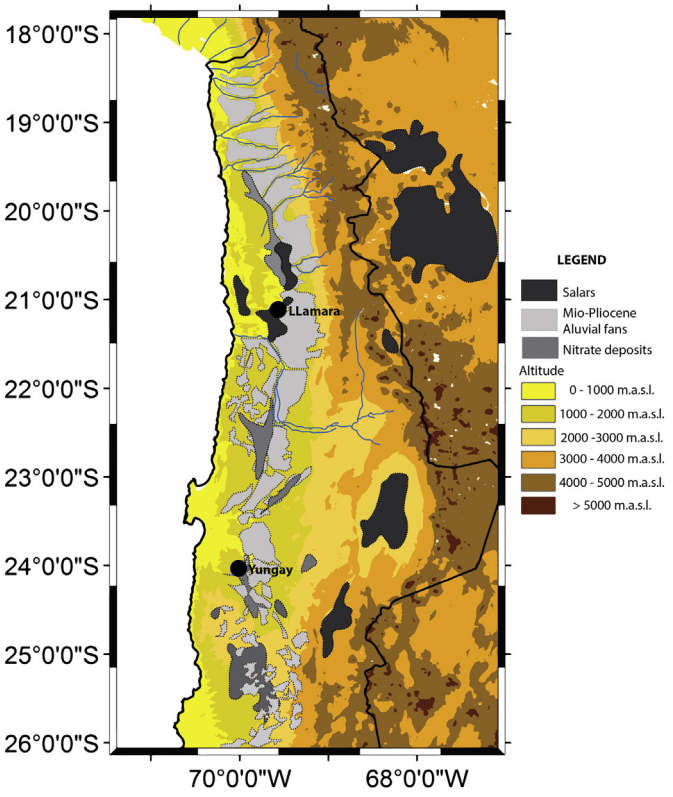

Fig. 2. Location of the Salar Llamara within the Atacama Desert, Chile. Salar deposits are shown in black, nitrate deposits in gray, and Mio-Pliocene alluvial fans in light gray. Figure from Finstad et al. (2014).

in this location. Radiocarbon dating of organic matter within the sediments revealed generally declining ages with decreasing depths, and distinctive age differences between the two sites. The Qh ages range from 12,209–15,484 cal yr BP, and samples from the Qp site range from 19,144–19,348 cal yr BP (Table 1).

Sites for soil excavations were selected for study based on examination of satellite imagery and field observations. A few open pits or stream exposures revealed that our sites appear to be representative of large regions of the landscape. Due to both the cost of sensors and the difficulty of excavation (which requires a jack hammer), we conducted the detailed research on one profile for each landform.

3. Materials and methods

3.1. Site description and soil sampling

Soils were excavated to depths of >1 m with the assistance of a portable jackhammer. Soil features were identified and described using methods outlined in the USDA Soil Survey Manual (Soil Survey Staff, 1999). Bulk soil samples of identified horizons were placed in zip lock bags and transported back to the lab. For the chemical and mineralogical measurements made here, this storage strategy likely had no effect on resulting data. Subsamples were taken in ~5 cm increments from the Bzm horizon of each soil for δ^{37}Cl analysis (Fig. 4). Three halite nodules from each site were also collected for subsequent study, and a groundwater sample was obtained from a backhoe trench that had been emplaced near the Qh site. Soil, halite nodules, and water samples were collected in June 2013. The chemical and isotopic analyses described below were conducted beginning in August 2013 and continued through February 2016.

Additionally, two radiocarbon ages obtained in 2009 (but previously unpublished) are included in the discussion to further constrain the timing and rates of lake drying and soil formation. This includes a

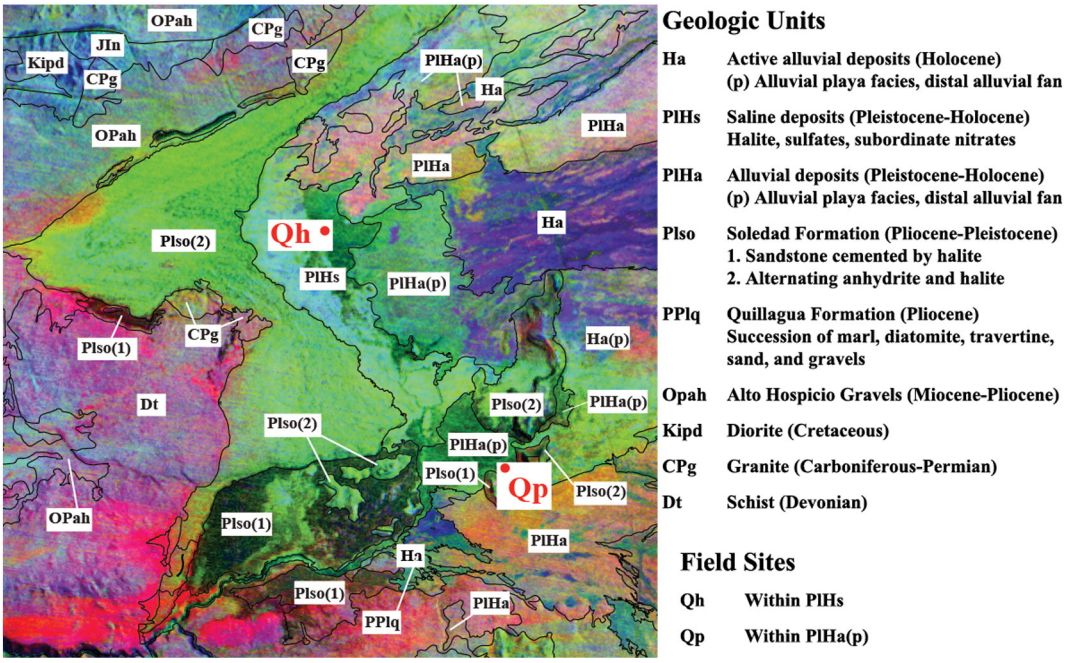

Fig. 3. Geological map of the region overlaid on a decorrelation stretch of Advanced Spaceborne Thermal Emission and Reflection Radiometer (ASTER) infrared bands 13, 12, and 11. Distribution of halite outcrops are shown in green. ASTER image courtesy of Matthew C. Jungers. Geological units were taken from Quezada et al. (2012). (For interpretation of the references to colour in this figure legend, the reader is referred to the web version of this article.)

sample of a salt-encrusted trunk of a bush or small tree from a coppice dune near the perimeter of the Qh salar, and a sample from a marl lens (at 50 cm depth) in a soil excavation at the periphery of the Qh salar, where the former wetland/lake transitioned to sand dunes, all of which are now encased in a thick halite crust.

3.2. Environmental monitoring

Decagon Devices Inc. (Pullman, WA) microclimate monitoring systems were installed at each site to track hourly fluctuations in air temperature, pressure, and relative humidity, and a leaf wetness sensor was installed to detect fog and dew condensation. Because it did not rain during the year of study, we assume that any "wetness" recorded by the leaf wetness sensor is due to dew formation on the surface. A value of 475 counts was chosen as the threshold for the presence of dew, which according to the manufacturer is a conservative threshold.

Seven Onset HOBO® Pro v2 (U23-002) temperature and relative humidity sensors were installed within halite nodules at each site, following the approach of Davila et al. (2008). Halite nodules were bored using an electric drill, and sensors (~1 cm) were inserted in the boreholes. Once a sensor was inserted into the crust, the hole was sealed with epoxy. The sensors were installed into the crust using slightly different methods at the two sites. At the Qh site, boreholes were made directly into the side of halite nodules. At the Qp site, an electric saw was first used to cut the nodule in half before sensor emplacement (Fig. 5). Removing half of the nodule using the saw (at the Qp site) allowed for the monitoring of denser crust located deeper within the nodule than would otherwise be accessible without first removing outer layers (at the Qh site).

An additional sensor was positioned just beneath the surface of one of the surface polygons (parallel to the surface) at each site. Three additional temperature and relative humidity sensors were placed at different depths within each soil, horizontally installed from the excavation walls. In total, the two uppermost soil sensors were inserted within the cemented halite horizons, while the lower two were in the fine-grained sediments. At the Qh site they were placed at 2, 20, 60, and 98 cm, and at the Qp site at 2, 37, 58, and 119 cm. All sensors were installed in June 2013 and ran continuously for 14 months.

In June 2013, the entire covering of halite nodules and surface crust was removed from a 1.5 m^2 plot at the Qh site. A Bushnell 119636C

Table 1
Radiocarbon dates from two samples from within the soil pits and three halite nodules from the surface. Additional dating was done from near the Qh site from a trunk of a carbonized bush on a salt encrusted coppice dune and from carbonate sample taken from a marl lens near the periphery of the shoreline. Radiocarbon ages were calibrated to calendar yr BP using the CALIBomb online program (http://calib.qub.ac.uk/CALIBomb/) with the dataset and extension curve corresponding to our study region (SH_CAL13; SHZ1–2) (Hogg et al., 2013; Hua et al., 2013).

Facility	Facility #	GPS	Site	Sample	Depth cm	δ13C (‰)	Δ14C	±	14C age cal yr BP	±
CAMS	166850	21°11′59.43″S 69°40′38.42″W	Qh	Halite	Surface	−25.44	9.3	3.0	modern	–
CAMS	166851	21°11′59.77″S 69°40′37.19″W	Qh	Halite	Surface	−24.77	8.8	3.3	modern	–
CAMS	166852	21°12′1.02″S 69°40′36.52″W	Qh	Halite	Surface	−24.89	7.4	3.0	modern	–
CAMS	165364	21°12′2.12″S 69°40′38.90″W	Qh	Qh 4	37–48	−27.43	−733.9	10.3	12209	817
CAMS	165162	21°12′2.12″S 69°40′38.90″W	Qh	Qh 10	94–96	−27.70	−801.4	1.9	15484	270
CAMS	166846	21°20′46.41″S 69°34′36.68″W	Qp	Halite	Surface	−29.41	−281.0	2.5	2546	54
CAMS	166847	21°20′46.92″S 69°34′36.18″W	Qp	Halite	Surface	−27.01	−623.5	2.9	8521	117
CAMS	166849	21°20′46.63″S 69°34′35.14″W	Qp	Halite	Surface	−25.99	−234.2	2.5	1995	68
CAMS	165159	21°20′45.46″S 69°34′37.56″W	Qp	Qp 5	65–82	−27.17	−865.2	2.0	19348	328
CAMS	165161	21°20′45.46″S 69°34′37.56″W	Qp	Qp 8	109–120	−26.80	−861.5	2.0	19144	302
UCIAMS	165230	21°12′26.81″S 69°38′19.97″W	near Qh	coppice dune bush trunk	surface	–	−72.4	1.8	547	17
Beta	263666	21°10′27.2″S 69°37′01.9″W	near Qh	marl lens	50	0.90	–	–	7343	79

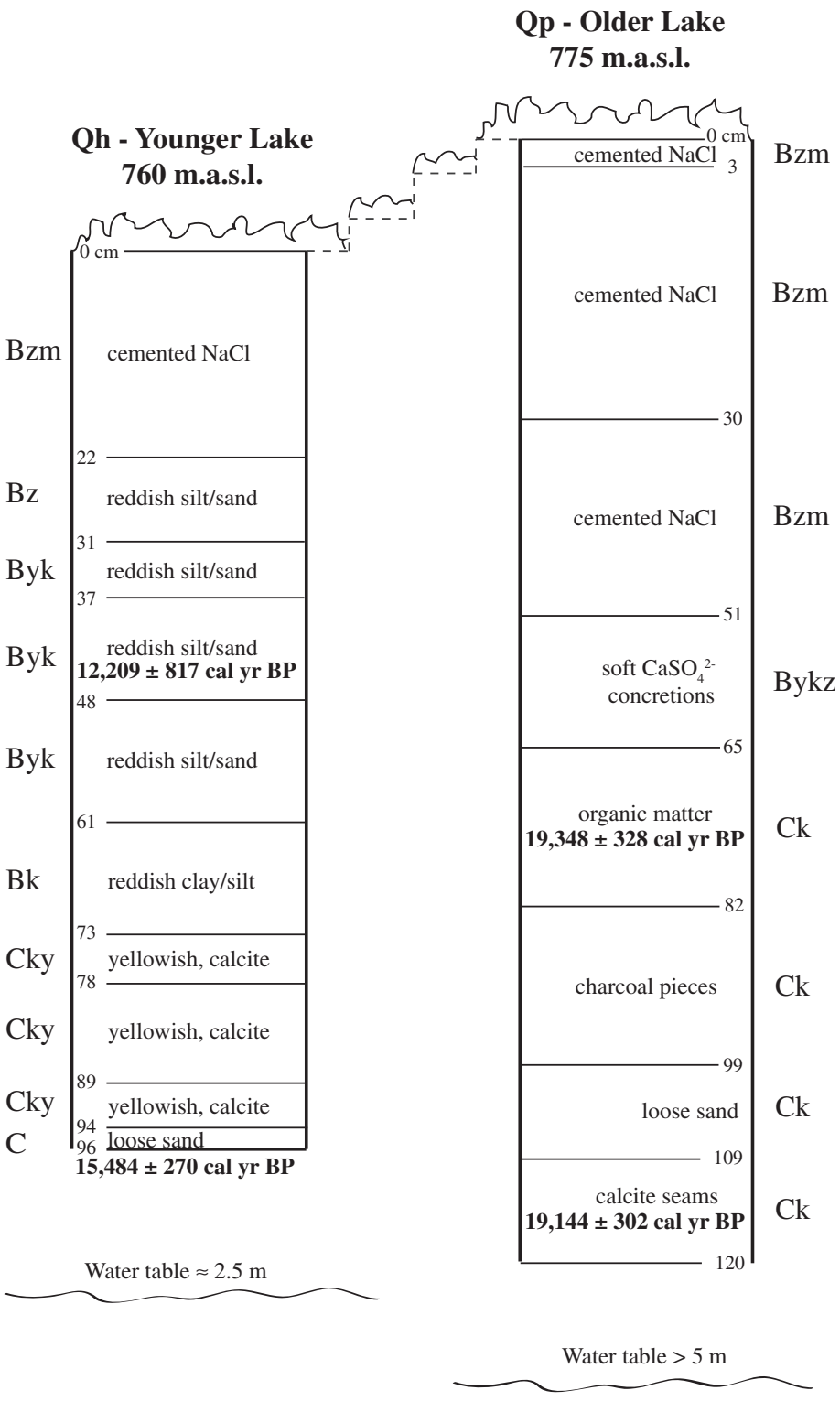

Fig. 4. Soil profiles from the Qh (younger) and Qp (older) sites. Soil features were identified and described using methods outlined in the USDA Soil Survey Manual (Soil Survey Staff, 1999) and both are classified as Gypsic Haplosalids. The water table at the Qh site was visible in a nearby backhoe trench at ~2.5 m. At the Qp site, the water table is believed to be >5 m. Radiocarbon dating details can be found in Table 1.

camera was then positioned to take a photograph every hour of the site to record the development and regeneration of new material. The camera was allowed to run for 2 years before photos were downloaded. After 14 months, a sample of the regenerated crust was removed and taken back to the lab for analysis.

3.3. Analytical methods

3.3.1. Soil chemistry and exchangeable salts

All soil samples, except those from Bzm horizons, were dried, sieved to <2 mm, and pulverized with a mortar and pestle. Soil samples from

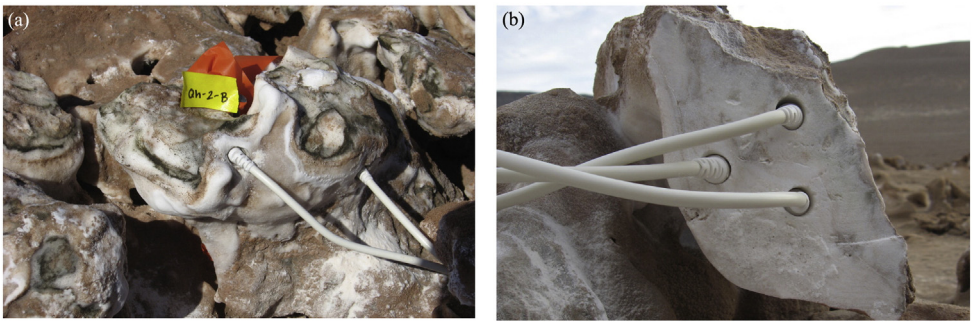

Fig. 5. Installation of temperature and relative humidity sensors within the halite nodules at each site. Sensors were installed directly into the side of nodules at the Qh site (a), and installed deeper within the nodule at the Qp site (b) after section the nodule with an electric saw. Approximate size of sensor is 1 cm diameter.

the Bzm horizons were dried and disaggregate in a mortar and pestle before being sieved to <2 mm and pulverized. Splits of each soil horizon were sent to ALS Geochemistry in Reno, NV for major and rare earth element concentration (CCP-PKG01) and measurement of Cl concentrations by nitric acid digestion and titration (CL-VOL66). Water extracts of the soil samples and the material that was removed from the regenerated surface crust at the Qh experimental plot were analyzed for SO_4^{-2} and Cl^- concentrations using a Thermo Scientific Dionex ICS1500 with an AS25 analytical column (ion chromatography) at UC Berkeley. Pulverized soil was dissolved in excess deionized water and shaken for 4 h to completely dissolve all salts. The samples were then filtered through a 0.2 μm filter and stored in a refrigerator at 2 °C for less than one week prior to analysis. Standards made from the Dionex Seven Anion Standard (No. 05790) were analyzed along with the samples. Calcium, potassium, and sodium in water extracts were determined using an ICP-OES in the College of Natural Resources at UC Berkeley. For these analyses, a portion of the water extracts prepared above was diluted in 2% HNO_3. Standards were created using Inorganic Ventures ICP standards CGNA1, CGK1, and CGCA1 and used to calculate final sample concentrations. The relative standard deviation (RSD) are better than 2% for each element based on daily analysis.

3.3.2. Radiocarbon measurements

Three halite nodule samples from each site were prepared for radiocarbon analysis by first removing inorganic carbon and excess salts in Nalgene bottles which had been soaked in an acid bath (0.4 M HCl) for 24 h followed by rinsing in deionized water. 20 g of pulverized halite was soaked in 1 M HCl for 24 h with intermittent shaking to agitate the solution, followed by centrifuging and decanting the acidic supernatant. To ensure complete removal of HCl, the samples underwent alternating soaking and shaking in deionized water for 24 h, then they were centrifuged and the supernatant discarded. This washing process with deionized water was repeated twice before samples were dried at 60 °C. A similar procedure was used to prepare two soil samples from each soil pit, with the exception that pulverized soil was soaked in 0.5 M HCl solution for inorganic carbonate removal. One carbonate sample from a marl lens near the Qh site was prepared for analysis by acid etch by Beta Analytics. The material was washed in deionized water to remove associated organic sediment and debris, then crushed and repeatedly subjected to HCl etches to eliminate secondary carbonate components.

Radiocarbon analysis of the soil pit and halite samples was performed on the Van de Graaff FN accelerator mass spectrometer (AMS) at the Center for Accelerator Mass Spectrometry at Lawrence Livermore National Laboratory, Livermore CA. Approximately 0.5 g of washed sample was prepared for ^{14}C measurement by sealed-tube combustion to CO_2 in the presence of CuO and Ag, and then reduced in the presence of H_2 at 570 °C (Vogel et al., 1984). Beta Analytic Inc. analyzed the carbonate sample from nearby the Qh pit by using an AMS after the reduction of sample carbon to graphite. The University of California, Irvine Keck Carbon Accelerator Mass Spectrometry facility analyzed the tree trunk sample from the coppice dune on a 500 kV compact AMS from National Electrostatics Corporation. $\delta^{13}C$ values were used to correct for fractionation and ^{14}C isotope values are reported in $\Delta^{14}C$ notation and corrected for ^{14}C decay since 1950 (Stuiver and Polach, 1977). Radiocarbon ages were calibrated to calendar yr BP using the CALIBomb online program (http://calib.qub.ac.uk/CALIBomb/) with the dataset and extension curve corresponding to our study region (SH_CAL13; SHZ1_2) (Hogg et al., 2013; Hua et al., 2013).

3.3.3. Sulfate stable isotope ratios

Sulfate S stable isotope ratio analysis was performed in the Laboratory for Environmental and Sedimentary Isotope Geochemistry at the Department of Earth and Planetary Science, UC Berkeley, following the protocol outlined in Michalski et al. (2004). Briefly, soil sulfate was dissolved in water by shaking pulverized soil for 4 h in 45 mL deionized water. The mass of soil ranged from 80 to 3000 mg, the sizes needed to precipitate 100 mg of $BaSO_4$, based on the total S content. Sediment was then removed by filtering through a 0.22 μm paper filter. Sulfate was precipitated as $BaSO_4$ by adding 5 mL 1 M $BaCl_2$ to the solution while samples were in a warm water bath (55 °C) under a standard laboratory fume hood. $BaSO_4$ was allowed to precipitate overnight. Samples were then centrifuged at 4000 rpm for 20 min and the supernatant was discarded. Precipitated $BaSO_4$ was then dried at 65 °C overnight. The same procedure was used to measure the groundwater sulfate isotope composition. Approximately 50–200 μg of $BaSO_4$ sample were analyzed in duplicate on a GV Isoprime isotope ratio mass spectrometer and a Eurovector Elemental Analyzer (EuroEA3028-HT), along with laboratory standards. The analytical precision of the measurement is better than 0.2‰. Values are reported as $\delta^{34}S$ relative to CDT.

3.3.4. Chlorine stable isotope ratios

The chlorine stable isotope composition of soil leachates and groundwater samples was determined in the Department of Geological Sciences, University of Texas at Austin. Chlorine was extracted from 1 g of pulverized soil by shaking in 50 mL ultrapure (18 MΩ) deionized water for 4 h, then filtering through a 0.2 μm filter. Samples were prepared following the procedures of Eggenkamp (1994) as modified by Barnes and Sharp (2006) and Sharp et al. (2007). Sulfur was removed as H_2S by adding 8 mL of 50% HNO_3 and heating for 3 h at 80 °C. Four mL of 1 M KNO_3 was then added to reach high ionic strength, followed by 1 mL of 0.4 M $AgNO_3$. AgCl was allowed to precipitate overnight in the dark then filtered through a glass fiber filter. The filter and precipitate were then inserted into a Pyrex tube and pumped to vacuum. Samples were reacted with 10 μL CH_3I to produce CH_3Cl. The tubes were sealed and allowed to react at 80 °C in the dark for 48 h before analysis. $\delta^{37}Cl$ values were measured on a ThermoElectron MAT 253 mass spectrometer and are reported in standard per mil notation vs. SMOC (Standard Mean Ocean Chloride; $\delta^{37}Cl$ SMOC = 0‰). Several duplicate samples from each site were run along with seawater standards which had been previously prepared. The analytical precision is ±0.14‰

based on the analyses of in-house seawater standards over the past year.

3.3.5. Carbonate stable isotope ratios

Carbonate C and O stable isotope analysis was performed in the Laboratory for Environmental and Sedimentary Isotope Geochemistry at the Department of Earth and Planetary Science, UC Berkeley. Pulverized soil samples were washed 3 times with deionized water to remove excess salts then dried at 50 °C overnight. 10–100 μg of calcite was analyzed using a GV IsoPrime mass spectrometer with a Dual-Inlet and MultiCarb system. Each unknown sample was run in duplicate and several replicates of the international standard (NBS19) and two internal lab standards (CaCO3-I & II) were measured during the run. The overall external analytical precision is ± 0.04‰ for $\delta^{13}C$ values and ± 0.07‰ for $\delta^{18}O$ values. $\delta^{13}C$ values are reported relative to V-PDB and $\delta^{18}O$ values relative to V-SMOW.

4. Results and discussion

4.1. Geological setting

While some of the NaCl crusts in salars of the region are of Neogene origins, field observations and radiocarbon dating of the soils examined here reveal that they have formed over late Pleistocene lacustrine deposits (see dating discussion which follows). Surrounding the outlines of the Qh salar, and in some places within the salar, there are salt-encrusted coppice dunes. A radiocarbon date from the carbonized trunk of a bush on one of these nearby dunes was 547 cal yr BP (Table 1). This suggests that both that the loss of surface water and the formation of salt indurated landscapes can and has occurred over a short geologic time frame.

Based on the boundary between flat lying sediments and salt encrusted coppice dunes, the "shoreline" of the Qh salar is located at ~760 m.a.s.l. Two radiocarbon constraints are available for this former wetland or lake. First, a radiocarbon measurement of a marl lens obtained from an excavation at 50 cm depth at the wetland periphery yields an age of 7343 cal yr BP (Table 1). Second, organic matter embedded in the apparently lacustrine sediments from our soil pits provided ages of 12,209 and 15,484 cal yr BP (Table 1).

The Qh basin is 10 to 15 m lower than surrounding remnants of an older lacustrine or marsh-like setting present at ~775 m.a.s.l. Organic material in fine-grained sediments in the soil yielded radiocarbon ages of 19,144 and 19,348 cal yr BP (Table 1). This unit has been dissected by streams draining to the present basin low point (Qh). The reasons for incision likely include both the ongoing tectonic tilting of the region (Allmendinger et al., 2005; Jordan et al., 2014) and the ongoing incision of the Quebrada Amarga, the drainage system that connects to the Rio Loa which drains to the Pacific. The ages of the organic material in the soils coincides with two well-documented wet periods known as the Central Andean Pluvial Events (CAPE), which activated stream discharge of the tributaries of the Salar Llamara (Nester et al., 2007). CAPE I occurred between 18,000 to 14,000 BP, while CAPE II was between 13,000 and 8500 BP (Gayo et al., 2012; Quade et al., 2008).

4.2. Soil profiles

Both soils are classified as Gypsic Haplosalids according to the USDA Soil Taxonomy (Fig. 4; Table 2). They each have a continuous cemented halite layer (Bzm) on the surface, though the thickness of this layer differs between sites. At the Qh site it spans 0–22 cm, and at the Qp site 0–51 cm. Beneath the Bzm layers the soil material is fine grained, with varying degrees of sand, silt, and clay. From 22 to 73 cm in the Qh profile, moist and soft layers of reddish silt and sand-rich material containing visible sulfate crystals were present. Further below this, yellowish horizons containing calcite were found at 73–94 cm, with loose sand below this at 94–96 cm.

Table 2
Soil chemistry data from excavations at both sites. Cation and anion concentrations from soil water extracts were measured at UC Berkeley using IC and ICP. Bulk soil major and trace elements concentrations are from ALS Chemex in Reno, NV.

Sample	Horizon	Depth	Na^+	K^+	Ca^{2+}	Cl^-	SO_4^{2-}	Cl	S	C	Al_2O_3	Fe_2O_3	SiO_2	TiO_2	CaO	K_2O	MgO	Na_2O	As	Se	Mo
		cm	mmol/g soil	mmol/g soil	mmol/g soil	mmol/g soil	mmol/g soil	wt.%	wt.%	wt.%	wt.%	wt.%	wt.%	wt.%	wt.%	wt.%	wt.%	wt.%	ppm	ppm	ppm
			Water extracts					Total chemistry													
Qh 1	Bzm	0–22	9.30	0.16	1.43	7.91	3.07	31.50	1.89	0.04	2.26	0.82	8.03	0.09	4.68	1.61	1.35	38.40	98.0	1.5	96
Qh 2	Bz	22–31	4.73	0.07	1.77	1.08	4.46	2.53	14.45	0.13	4.70	1.82	15.60	0.18	16.10	1.23	2.33	14.05	>250	0.7	87
Qh 3	Byk1	31–37	0.14	0.02	2.62	0.15	3.38	0.50	14.20	0.48	5.60	2.18	17.60	0.21	27.30	1.32	1.67	1.68	190.0	0.7	9
Qh 4	Byk2	37–48	0.05	0.02	2.60	0.06	3.10	0.12	16.25	0.37	4.11	1.60	13.05	0.15	30.70	0.94	1.24	0.54	146.5	0.5	2
Qh 5	Byk3	48–61	0.01	0.02	1.45	0.02	1.68	0.04	6.30	0.38	12.60	4.81	38.30	0.50	12.75	2.65	2.26	0.95	171.0	0.5	3
Qh 6	Bk	61–73	0.00	0.02	0.17	0.03	0.28	0.03	0.77	1.31	15.60	6.11	49.90	0.63	7.72	3.21	2.73	1.22	171.5	0.7	6
Qh 7	Cky1	73–78	0.00	0.00	2.68	0.01	3.19	0.02	15.90	2.40	1.34	0.62	5.39	0.05	40.10	0.30	0.76	0.19	143.5	0.6	3
Qh 8	Cky2	78–89	0.00	0.00	2.70	0.01	3.21	0.02	17.00	2.21	0.66	0.31	3.34	0.03	40.60	0.15	0.64	0.12	95.7	0.4	2
Qh 9	Cky3	89–94	0.00	0.00	2.61	0.01	3.08	0.03	14.50	0.96	3.92	1.49	18.50	0.18	30.50	0.75	0.86	0.74	95.2	0.5	7
Qh 10	C	94–96	0.00	0.01	1.30	0.03	1.51	0.03	4.72	0.14	11.55	4.13	53.00	0.56	9.75	2.30	1.54	1.69	91.6	0.6	5
Qp 1	Bzm1	0–3	7.06	0.00	0.12	8.09	0.23	15.60	0.36	0.25	9.35	2.30	49.60	0.30	3.49	1.81	0.77	16.35	21.8	1.9	5
Qp 2	Bzm2	3–30	10.64	0.07	0.07	9.06	1.07	29.40	1.44	0.32	5.56	1.87	19.45	0.22	2.02	1.34	0.82	33.30	15.7	3.4	15
Qp 3	Bzm3	30–51	16.76	0.04	0.11	11.27	0.99	18.35	1.61	0.35	7.84	2.58	33.40	0.31	2.67	1.73	0.98	23.30	20.8	2.7	12
Qp 4	Bykz	51–65	4.98	0.01	0.11	0.66	2.46	1.21	6.77	0.55	10.85	3.81	38.20	0.44	3.26	1.97	1.66	14.85	29.5	1.4	5
Qp 5	Ck1	65–82	1.15	0.00	0.05	0.80	0.55	1.40	1.57	0.76	14.30	5.05	52.30	0.63	4.67	2.31	2.06	6.06	32.2	1.2	6
Qp 6	Ck2	82–99	0.99	0.00	0.16	0.54	0.62	0.87	1.86	0.61	13.85	4.70	55.60	0.57	4.89	2.53	1.92	5.37	34.4	1.2	7
Qp 7	Ck3	99–109	0.24	0.00	0.18	0.22	0.34	0.36	1.01	0.40	12.80	3.31	65.90	0.41	4.17	2.45	1.16	3.90	21.9	0.7	4
Qp 8	Ck4	109–120	0.41	0.00	0.23	0.55	0.41	0.80	1.24	0.61	13.65	4.55	56.80	0.58	5.06	2.52	1.87	3.63	42.8	1.2	7

The Qp site has a similar soil chemical sequence. Beneath the Bzm horizon, soft sulfate concentrations were observed from 51 to 65 cm. Deeper in the profile from 65 to 99 cm, organic material and charcoal pieces were present within moist and soft layers of variegated black, orange, and gray. A horizon of loose sandy material was observed from 99 to 109 cm, and 109–120 cm was comprised of variegated brown material with calcite seams.

Most playas and saltpans undergo repeated cycles of wetting and drying as the surface receives precipitation during seasonally wet months and evaporation of this water during the dry months. This cycle is well-documented to create stratigraphic profiles with alternating mud from the flooding of the surface, and halite layers deposited during evaporation (Lowenstein and Hardie, 1985). The sequence of soil horizons in the Qh and Qp sites do not show this alternating pattern, rather they have evaporitic horizons concentrated at the surface and the fine grained siliceous material concentrated deeper in the profile. This is indicative that this salar has not undergone repeated cycles of wetting and drying, but instead has been continuously drying since the final stages of lake/marsh evaporation.

A groundwater lens was present at the Qh excavation, and a nearby backhoe pit suggests that the local water table is at ~2.5 m below the surface. In contrast, groundwater was not observed at the Qp location, which must be >5 m below the surface based on the absence of water in nearby incised stream channels. However, both the soil excavation and natural exposures along the incised stream channels revealed moist sediment. Rates of evaporation are highly dependent on the depth of the groundwater, with shallower water leading to more rapid evaporation (Houston, 2006). A more detailed discussion on the rates of salt accumulation and evaporation can be found later in Sections 4.3 and 4.4.

4.3. Soil water flux

There are strong water gradients in the upper 1.5 m of both soils as revealed by the relative humidity sensors placed within the excavation pits. It is apparent that the Qh profile has a higher water content at all measured depths than the Qp soil (Table 3; Fig. 6). The relative humidity sensors show that from 60 cm and below, the Qh soil maintains 100% relative humidity year-round. In comparison, sensors in the Qp soil indicate an average yearly relative humidity of 79% at 58 cm and 87% at 119 cm depths. The relative humidity profiles in both soils are indicative of upward water flow from evaporative removal of groundwater, with a higher rate of evaporation at the Qh site. To quantify this, Fick's law was used to calculate the isothermal vertical transport of water vapor in each soil (Bittelli et al., 2008):

$$q'_v = -D_v\left(\frac{dc_v}{dz}\right) \quad (1)$$

where D_v is the vapor diffusivity in soil ($m^2\ s^{-1}$) and c_v is the soil vapor concentration ($g\ m^{-3}$) calculated as

$$c_v = hc'_v \quad (2)$$

where h is the fractional relative humidity and c'_v is the saturation vapor concentration ($g\ m^{-3}$). The average relative humidity values from soil pit sensors over the 14-month monitoring period were used to determine c_v, using Eq. (2) with a c'_v of 17.29 ($g\ m^{-3}$) at 20 °C. Calculations for q'_v were done assuming a D_v of 2.39×10^{-5} ($m^2\ s^{-1}$) (Weisbrod and Dragila, 2006). With these parameters, Eq. (1) yielded q'_v values of −0.044 and −0.028 L $m^{-2}\ d^{-1}$ at the soil-atmosphere interface from the Qh and Qp soils, respectively (Table 4). These estimated flux values are discussed further in the following section.

4.4. Rates of soil formation and groundwater evaporation

By making inventories of the total salt accumulation divided by the age of the soils, we can estimate the long-term rates of evaporation and associated salt deposition, and compare these values to the estimates made using vapor diffusion above. We use maximum ages of 15,484 and 19,348 cal yr BP for the Qh and Qp sites, respectively, while recognizing that lake/wetland cessation may have occurred much later than when the sediment itself accumulated. Horizon depth and Cl concentration data were used to determine the mass of NaCl in each soil (Table 2). Assuming a bulk density of 1.50 g cm^{-2}, there are 135,450 g Cl m^{-2} at Qh, and 197,393 g Cl m^{-2} at Qp, which is equivalent to 222,550 and 324,758 g NaCl, respectively. These data suggest that the soils have both accumulated NaCl at similar rates over geologic time (~9 g $m^{-2}\ y^{-1}$ and ~10 g $m^{-2}\ y^{-1}$).

It is likely, however, that evaporation rates have not remained constant over time. Kampf et al. (2005) suggested that rates of groundwater evaporation from playas may slow over time as the thickness of the salt crust increases. To test this hypothesis, and to better understand the present dynamics of this environment, we removed (as completely as possible using a jackhammer) an area of the halite crust in the vicinity of site Qh and monitored its renewal over a multi-year period using both time-lapse photography and salt accumulation measurements. After one year a subsample of this newly formed crust was removed and taken back to the lab for analysis. Approximately half of the material was salt, with 0.26 g Cl^- and 0.21 g SO_4^{2-} per gram of crust. This very short-term rate of halite accumulation was approximately 458 g m^{-2}, a rate ~38× faster than the estimated geological rate of accumulation.

The Cl^- in the groundwater near the Qh site has a concentration of 0.9 g L^{-1}, 4× higher than a nearby spring with a concentration of 0.2 g L^{-1} (Magaritz et al., 1989). At the measured concentration of 0.9 g L^{-1}, the evaporation of over 219,000 L m^{-2} of water is required to accumulate the current mass of NaCl at Qp, over 150,000 L m^{-2} of water at Qh, and 510 L m^{-2} at the Qh experimental site. This is equivalent to rates of evaporation of 0.031 mm $m^{-2}\ d^{-1}$ at the Qp site, 0.027 mm $m^{-2}\ d^{-1}$ at the Qh site, and 1.19 mm $m^{-2}\ d^{-1}$ at the experimental site (Table 4). These values are well aligned with the values for water flux calculated using relative humidity gradients and Fick's law in

Table 3
Average seasonal temperature and relative humidity from within the soil pits. Onset HOBO® Pro v2 (U23-002) sensors were installed at 2, 20, 60, and 98 cm at the Qh site, and at 2, 37, 58, and 119 cm at the Qp site in June 2013 and run for 14 months.

	Dec–Feb		Mar–May		Jun–Aug		Sep–Nov		Entire year	
	avg T °C	avg RH %	avg T °C	avg RH %	avg T °C	avg RH %	avg T °C	avg RH %	avg T °C	avg RH %
Qh 2 cm	26	32	21	37	15	47	22	34	20	38
Qh 20 cm	26	68	21	71	16	75	22	72	21	72
Qh 60 cm	24	100	22	100	18	100	21	100	21	100
Qh 98 cm	23	100	22	100	19	100	20	100	21	100
Qp 2 cm	29	25	24	32	18	37	24	25	23	30
Qp 37 cm	26	62	22	65	16	68	22	64	21	65
Qp 58 cm	26	79	23	79	18	79	22	79	22	79
Qp 119 cm	25	87	24	86	20	88	22	88	23	87

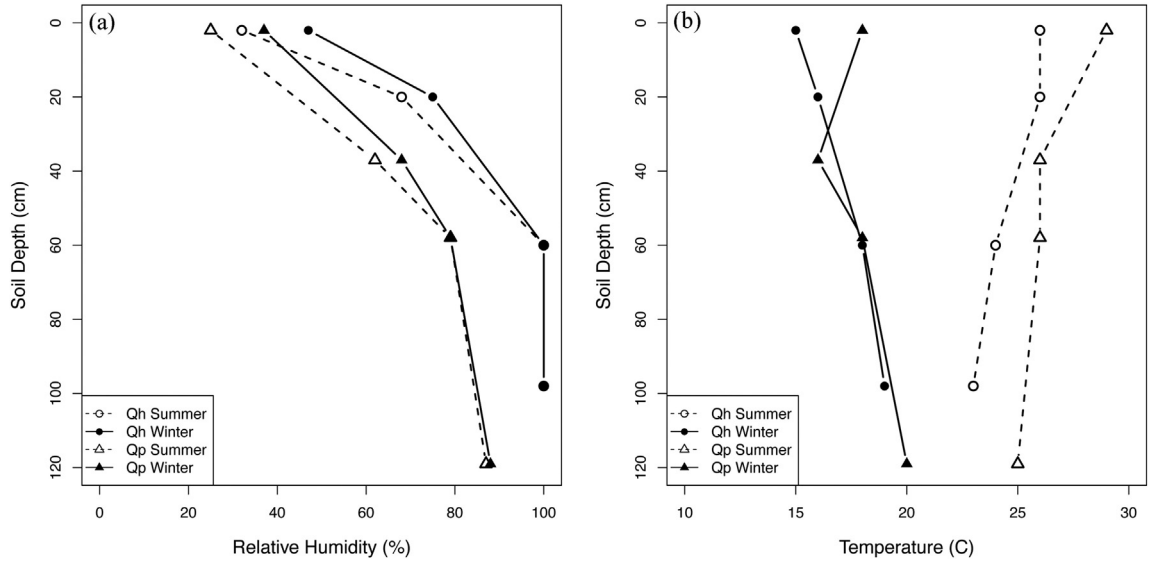

Fig. 6. Average relative humidity (a) and temperature (b) profiles in the soil pits from sensors at 2, 20, 60, 98 cm at the Qh site and 2, 37, 58, 119 cm at the Qp site. Summer includes Dec., Jan., and Feb., winter includes Jun., Jul., Aug. Additional data can be found in Table 3.

Section 4.3. Kampf et al. (2005) reported a range of evaporation rates from the Salar de Atacama in Chile, a salar at a much higher and more inland elevation than the Salar Llamara. Sites with thick salt crusts showed negligible evaporation and were considered to be hydrologically sealed, whereas unvegetated sites with bare soil had evaporation rates of 1 mm d^{-1}. Our results are generally consistent with these rates and their conclusions from the Salar de Atacama data that show that evaporation rates are time, and degree of soil development, dependent.

To better understand the rate and processes of surface crust formation we installed a time-lapse camera to take pictures of the experimental site on a regular basis (Fig. 7). The photo time series visually reveals how rapidly the salt crust can be generated from a relatively thin starting point. The photos shown here are all taken from approximately the same time of day. It is apparent that wetting occurs on a regular basis from fog or dew. Areas impacted by wetting are noted with circles and boxes on the photographs, and appear to be concentrated on relatively higher areas. These areas also appear to show the fastest growth or visual modification. Once an area begins to form a crust, it appears to be preferentially wetted during subsequent fog events, possibly because it is higher off the ground than surrounding areas and/or is purer in NaCl. As time passes, the amount of surface area that appears wet in each photograph continues to grow. In the final picture, cracks filled with salt are becoming apparent (noted with arrows), with fresh salt deposits evident by the bright white colour.

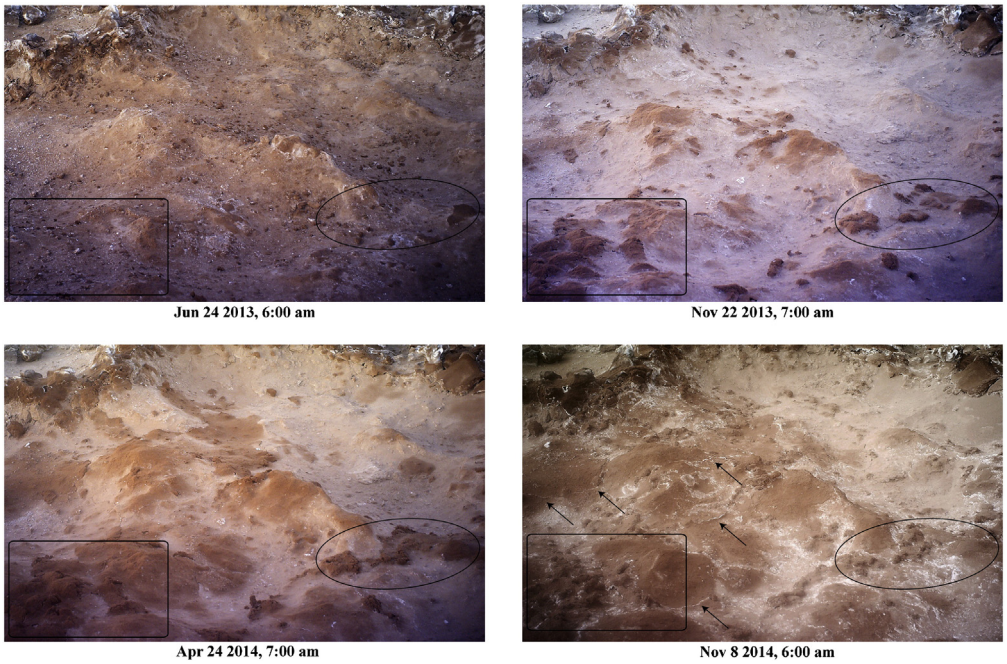

Fig. 7. Selected images from time-lapse camera placed at Qh experimental site. Surface crust was completely removed from a 1.5 m^2 plot in June 2013. Photos were taken hourly for 2 years to record development and regeneration of new material. Locations of fastest growth are indicated with circle/square outlines. Cracks filled with fresh (white) salt are noted with arrows.

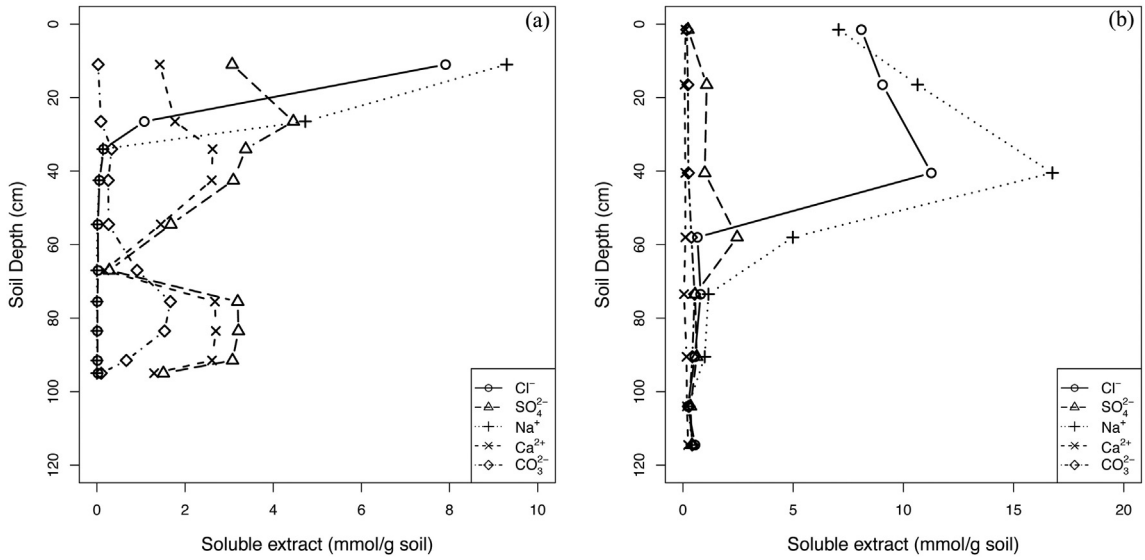

Fig. 8. Depth profiles of ions in the Qh soil (a) and Qp soils (b). Chloride and sulfate concentrations in water extracts were analyzed by IC. Sodium and calcium concentrations in water extracted were analyzed by ICP. Carbonate concentrations were calculated from total wt% C data (Table 2).

4.5. Observed and modeled salt profiles

4.5.1. Profiles of salt minerals

The relative humidity profiles in the soils indicate upward transport of water vapor. Evaporative vapor movement and capillary liquid flow are the main mechanisms by which salt moves and precipitates (Ericksen and Salas, 1990). As water moves upward and is removed by evaporation, salts are deposited as their solubility coefficients are exceeded. Carbonates are deposited first, followed by sulfates, and finally halides. This sequence also occurs in well-drained desert soils, but there the water flow is downward and the depth sequence is reversed (Finstad et al., 2014).

Water extracts of the soil reflect the pore water chemistry, and reveal the distribution of pore water salts with depth (Fig. 8; Table 2). Both soils have a dense, cemented halite soil horizon on the surface and have decreasing water extractable sodium and chloride concentrations with decreasing depth (halite solubility = 360 g L^{-1}). The maximum extractable sulfate concentration occurs beneath the halite layer. In the Qh soil, soluble sulfate peaks at 22–48 and 73–94 cm, and soluble calcium concentrations mirrors the sulfate throughout the profile (gypsum solubility = 2.1 g L^{-1}). Soluble sulfate in the Qp soil reaches maximum values at 30–65 cm. In this soil, there is a weaker correlation between sulfate and calcium, and soluble calcium is mostly invariant with depth. Sodium is the only soluble cation present in large quantities within the sulfate layer, suggesting that mirabilite ($NaSO_4 \cdot 10H_2O$) may be forming in the Qp soil (mirabilite solubility = 274 g L^{-1}).

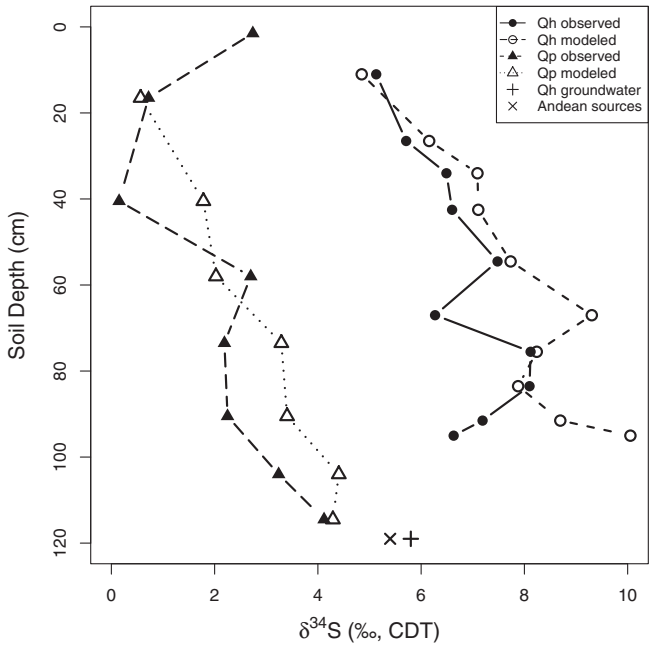

Fig. 9. Measured and modeled $\delta^{34}S$ values from extractable sulfate at both sites with depth. A groundwater sample from the Qh site is included, as well as Andean weathering sources from Rech et al. (2003). Modeled values were calculated using Rayleigh fractionation following Ewing et al. (2008). All values are reported relative to CDT.

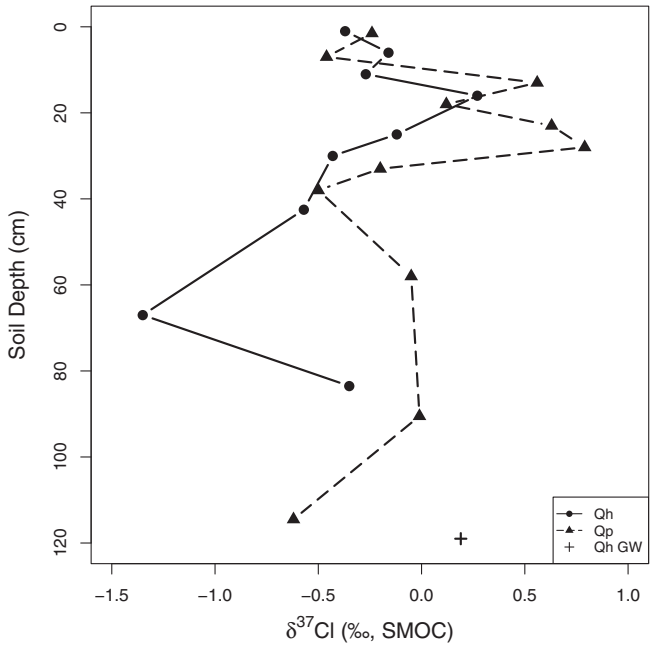

Fig. 10. $\delta^{37}Cl$ values of extracted soil water at both sites with depth. A groundwater sample from the Qh site is included and ~5 cm subsamples of the Bzm horizons (cemented halite). All samples are reported relative to SMOC.

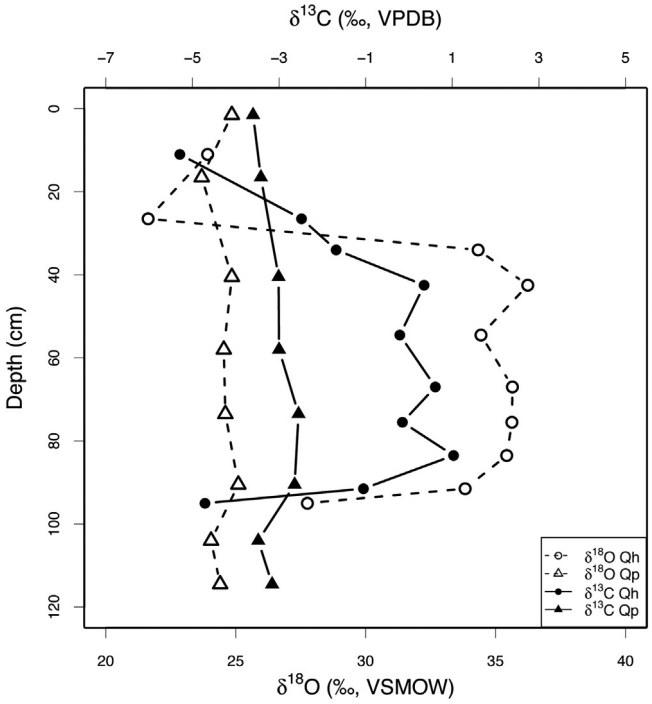

Fig. 11. $\delta^{13}C$ and $\delta^{18}O$ values of carbonates at both sites with depth. $\delta^{13}C$ (top axis) is reported relative to VPDB and $\delta^{18}O$ (bottom axis) is reported relative to VSMOW.

Carbonates were observed in the lower segments of the soils. In the Qh soil, carbonate peaks at 61–94 cm, with >2% total carbon in the solid phase, and soluble Ca mirrors this trend, indicating that $CaCO_3$ is the dominant mineral (calcite solubility = 0.05 g L^{-1}). In the Qp soil, carbonate was present in low concentrations (0.3–0.8% C) throughout much of the profile, though the highest concentrations are found from 51 to 99 cm (0.6–0.8% C). We recognize that not all the carbonate is likely to be pedogenic, since observations of these sediments show that they contain lacustrine carbonate (see Section 4.5.4). Isotopes from all these salts can provide more information on their origin, and provide insights into the transport processes that have emplace them in the soils.

4.5.2. Sulfate stable isotope ratios

The sulfate dissolved in groundwater near the Qh site has a $\delta^{34}S$ value of 5.54‰ (Table 5). Possible sulfate sources to these soils are weathering of Andean volcanic rock and marine inputs. Rech et al. (2003) report that Andean mantle and juvenile rocks have $\delta^{34}S$ values of −5 to +5‰. In contrast, biogenic marine sulfates have $\delta^{34}S$ values of +13 to +22‰, and seawater sulfate a $\delta^{34}S$ value of about +21‰ (Bao et al., 2000). In the region of the soils discussed here, there are large outcrops of Miocene-aged anhydrite that are part of the locally important Soledad formation (Pueyo et al., 2001). This ancient sulfate accumulated at the terminal end of the ancestral Rio Loa, which likely obtained most of its solutes from Andean sources. Thus, the groundwater sulfate we measured appears to largely reflect lithological sources of S.

The $\delta^{34}S$ value of sulfate in both soils generally increases with depth (Fig. 9; Table 5). The weighted average $\delta^{34}S$ value of sulfate in the exposed profiles is 6.47‰ and 1.71‰ for the Qh and Qp sites, respectively. $\delta^{34}S$ values in the Qh soil ranged from 5.1‰ to 8.1‰, and the Qp ranged from 0.2 to 4.1‰. For comparison, both of these soils have $\delta^{34}S$ values within the range reported by Ewing et al. (2008), who studied a soil formed on an alluvial fan south of the Salar Llamara. There, the total soil sulfate averaged 3.7‰, and ranged from 0 to 9.6‰, with values decreasing with increasing depth. The sulfur inputs in that location are from atmospheric deposition, as opposed to the groundwater sources as examined here. However, the similarity in average values between these two studies emphasizes the overwhelming impact of volcanic sulfur on the regional sulfur cycle in the interior of the desert.

The stable S isotope composition of sulfates provides evidence of the direction of solute flow (Amundson et al., 2012; Ewing et al., 2008). Due to small isotopic differences between the dissolved and solid phases of

Fig. 12. Picture of the Qp site illustrating the surface cracking and polygonal shape. Halite nodules are observed surrounding the polygons coming up from surface cracks.

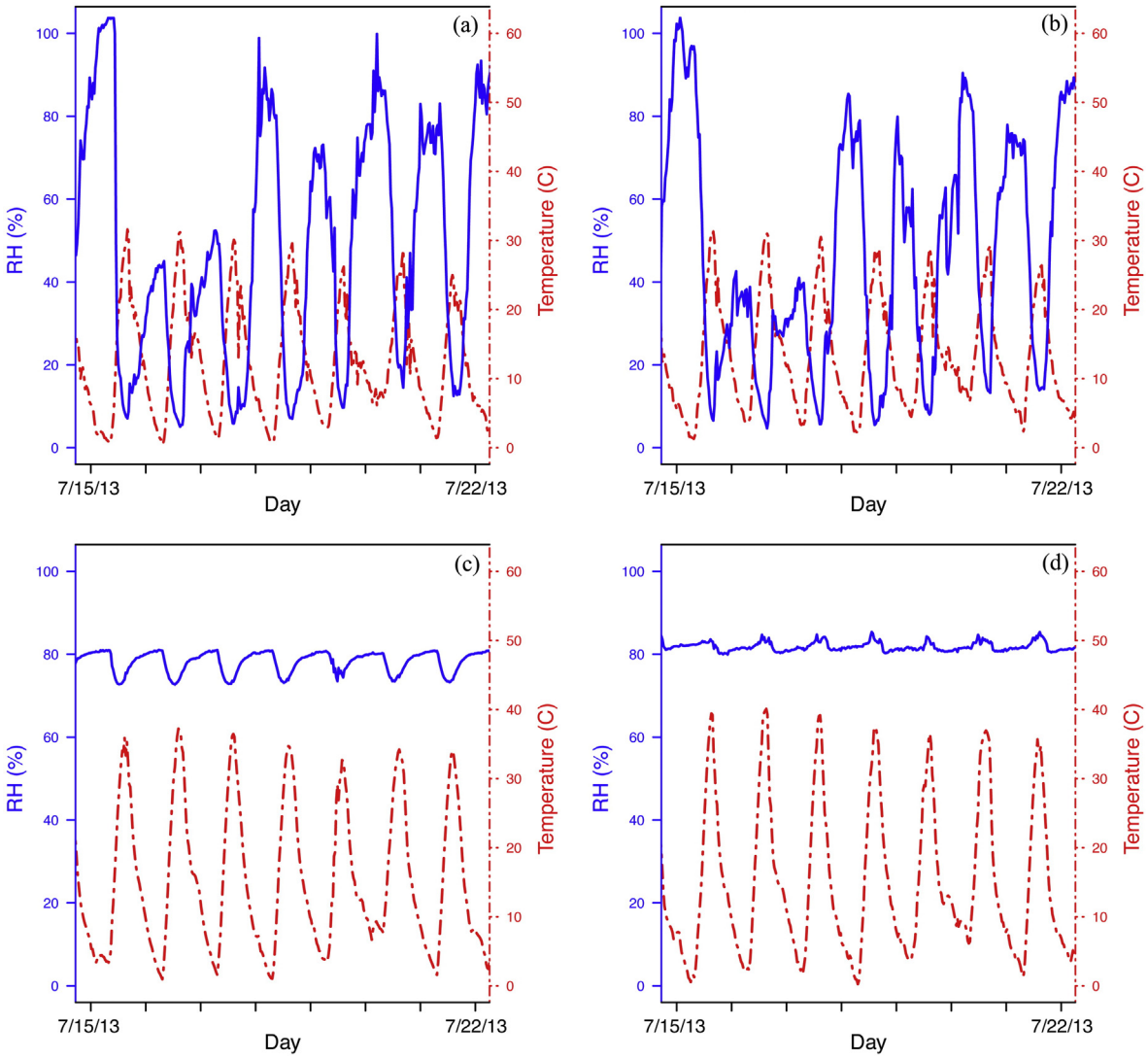

Fig. 13. Temperature and relative humidity data for one week in July 2013. Each tick mark on x-axis indicates 24 h. Atmospheric conditions from the Qh site (a), atmospheric conditions from Qp site (b), a selected halite nodule from Qh (c), and a selected halite nodule from Qp (d). RH within halite nodules (c and d) remains constant even when atmospheric RH (a and b) are below 50%.

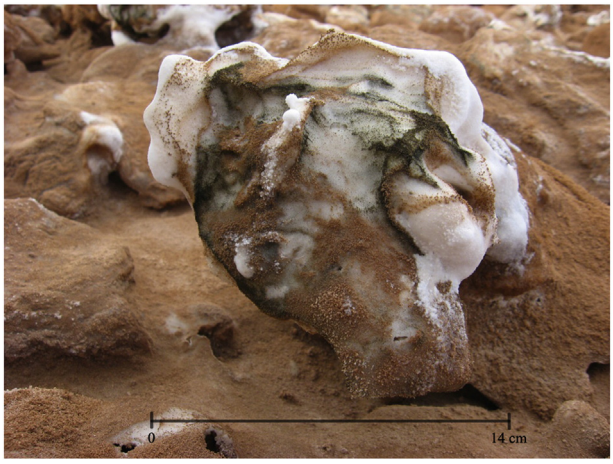

Fig. 14. Halite nodule with visible growth of microbial communities (dark green banding on surface). (For interpretation of the references to colour in this figure legend, the reader is referred to the web version of this article.)

sulfate, combined with the downward migration of remaining soluble sulfate, the S isotope composition of solid phase sulfate tends to decrease in the direction of fluid flow, a trend that can be described by a Rayleigh fractionation model. Ewing et al. (2008) were able to apply this model to mimic the S isotope profile of a Pliocene-aged soil formed by the downward migration of infrequent rainfall. The soil displayed a nearly 10‰ decrease in $\delta^{34}S$ values with depth, due to the downward movement of water and the preferential transport of ^{32}S to greater depths over time.

Here, we use this model to determine how these processes apply in the case of upward migrating water and solutes. Following Ewing et al. (2008), sulfate fractionation was calculated using a Rayleigh model (Criss, 1999):

$$\delta_{solid}(z) = \left(\delta_{inputs}(z) + 1000\right) f^{\,\alpha_{w-s}-1}) - 1000 \quad (3)$$

where $\delta_{solid}(z)$ is the δ value for the solid at depth z, $\delta_{inputs}(z)$ is the δ value of the dissolved inputs at depth z, f is the sulfate inventory at z as a fraction of the total inventory above depth z, and $\alpha_{w\text{-}s}$ is the

Table 4
Rates of water evaporation from both soils calculated from Cl accumulation and Fick's Law. Total Cl deposition was calculated assuming a bulk density of 1.50 g cm^{-2} and using total % Cl (Table 2). Rates of Cl deposition was calculated using the max ages from each soil pit (Table 1). Rates of water evaporation were calculated assuming a groundwater Cl concentration of 0.9 g L^{-1} as measured from the Qh groundwater and the max ages from each soil pit. Calculations for dC_v/dz. were done at z = 0 using gradients of relative humidity from sensors (Table 3), and q'_v was calculated assuming a D_v of 2.39×10^{-5} (m^2 s^{-1}) (Weisbrod and Dragila, 2006).

Site	Soil age	Total Cl deposition	Cl deposition rate	Total water evaporated	Water evaporation rate	dC_v/dz	q'_v
	cal yr B.P.	g m^{-2}	g m^{-2} y^{-1}	L m^{-2}	mm m^{-2} d^{-1}	g m^{-2}	L m^{-2} d^{-1}
	Measured	Calculated from % Cl	Calucated from salt accumluation rates			Calculated from Fick's Law	
Qh	15,484	135,450	8.75	150,500	0.027	21.39	-0.044
Qp	19,348	197,393	10.20	219,325	0.031	13.76	-0.028
Experimental	1.17	536	458	510	1.19	–	–

fractionation factor for precipitated sulfate (1.65‰ at 21 °C; Thode and Monster (1965)). $\delta_{inputs}(z)$ was calculated by mass balance:

$$\delta_{inputs}(z+1) = \frac{\delta_{inputs}(z)SO4^{2-}_{inputs}(z) - \delta_{solid}(z)SO4^{2-}_{solid}(z)}{SO4^{2-}_{diss}(z)} \quad (4)$$

where $SO4^{2-}_{inputs}(z)$ is the mass of sulfate per area being added, $SO4^{2-}_{solid}(z)$ is the mass of sulfate per area precipitated as a solid, and $SO4^{2-}_{diss}(z)$ is the mass of sulfate per area remaining in the dissolved phase. Since water movement (and therefore solute transport) is assumed to be rising up through the profile, calculations were performed using the base of the soils at z = 0. The input at z = 0 is the total inventory of salt in the soil and its weighted mean isotopic composition.

The model calculations are compared to the measured $\delta^{34}S$ values in Fig. 9 and Table 5. Both soils show marked decreases in $\delta^{34}S$ values with decreasing depth. The model results mirror the depth trend for the Qp soil, and also closely mimic the $\delta^{34}S$ values of the Qh soil in the upper 55 cm. Below this depth, the model less accurately reflects the $\delta^{34}S$ values. One possible explanation for the divergence from the model at the greater depths is the high and constant soil moisture. The Rayleigh model is based on the assumption that the $\delta^{34}S$ values are driven by repeated deposition and reprecipitation as the soil undergoes wetting and drying cycles. Relative humidity sensors indicate that from 50 cm and below, this soil is at 100% relative humidity year-round, which would impede dissolution and reprecipitation.

When the two sites are compared, the greatest difference is that the $\delta^{34}S$ in the Qp soil is approximately 5‰ more negative than that of the Qh. One explanation for this is the different lengths of chemical evolution pathways for the soils (e.g., depth to water table). Sulfate must migrate from much greater depths at the Qp site, and therefore undergoes chemical evolution over a greater distance. Possibly supporting this notion is the observation that the Qp soil has about half the concentration of sulfate as the Qh soil. Alternatively, there could be a slight difference in ground water sources in the basin, but we are unable to test this possibility.

Table 5
Stable isotope compositions with depth, including $\delta^{37}Cl$ and $\delta^{34}S$ from the Qh groundwater. $\delta^{37}Cl$ and $\delta^{34}S$ values are from extracted soil water, $\delta^{13}C$ and $\delta^{18}O$ are from bulk soil. Subsamples from the Bzm (cemented halite) horizon were included for Cl isotope analysis to capture smaller scale fractionation (~5 cm). Modeled $\delta^{34}S$ values were calculated using Rayleigh fractionation following Ewing et al. (2008).

Sample	Depth	$\delta^{37}Cl$ Chlorine	$\delta^{34}S$ Sulfate	$\delta^{34}S$ Sulfate	$\delta^{13}C$ Carbonate	$\delta^{18}O$ Carbonate
	(cm)	(‰, SMOC)	(‰, CDT) Measured	(‰, CDT) Modeled	(‰, VPDB)	(‰, VSMOW)
Qh 1	0–22	–	5.13	4.85	−5.29	23.92
Qh 1a	1	−0.34	–	–	–	–
Qh 1a	1	−0.40	–	–	–	–
Qh 1b	6	−0.16	–	–	–	–
Qh 1c	11	−0.27	–	–	–	–
Qh 1d	16	0.27	–	–	–	–
Qh 2	22–31	–	5.71	6.16	−2.48	21.63
Qh 2a	25	−0.12	–	–	–	–
Qh 2b	25	−0.31	–	–	–	–
Qh 2b	30	−0.43	–	–	–	–
Qh 3	31–37	–	6.49	7.09	−1.68	34.33
Qh 4	37–48	−0.57	6.60	7.11	0.35	36.24
Qh 5	48–61	–	7.48	7.73	−0.21	34.44
Qh 6	61–73	−1.44	6.27	9.31	0.61	35.65
Qh 6	61–73	−1.26	–	–	–	–
Qh 7	73–78	–	8.12	8.24	−0.15	35.63
Qh 8	78–89	−0.35	8.10	7.88	1.03	35.43
Qh 9	89–94	–	7.19	8.70	−1.05	33.83
Qh 10	94–96	–	6.63	10.05	−4.71	27.76
Qh GW	~2.5 m	0.19	5.54	–	–	–
Qp 1	0–3	−0.18	2.74	–	−3.60	24.85
Qp 1	0–3	−0.29	–	–	–	–
Qp 2	3–30	–	0.72	0.57	−3.42	23.69
Qp 2a	7	−0.46	–	–	–	–
Qp 2b	13	0.56	–	–	–	–
Qp 2c	18	0.12	–	–	–	–
Qp 2d	23	0.63	–	–	–	–
Qp 2e	28	0.79	–	–	–	–
Qp 3	30–51	–	0.15	1.78	−3.01	24.85
Qp 3a	33	−0.42	–	–	–	–
Qp 3a	33	0.01	–	–	–	–
Qp 3b	38	−0.50	–	–	–	–
Qp 4	51–65	−0.05	2.70	2.03	−3.00	24.54
Qp 5	65–82	–	2.19	3.29	−2.55	24.60
Qp 6	82–99	−0.01	2.25	3.40	−2.64	25.10
Qp 6	82–99	−0.06	–	–	–	–
Qp 7	99–109	–	3.24	4.41	−3.48	24.05
Qp 8	109–120	−0.62	4.12	4.29	−3.16	24.40

4.5.3. Chlorine stable isotope ratios

The stable chlorine isotope composition of NaCl provides information on the geologic source of the chlorine and, in certain geochemical settings, information on the mechanism and direction of soil water flow (Amundson et al., 2012). Amundson et al. (2012) found that in a cold desert of Antarctica where brines move along thermal gradients, diffusional movement of chlorine imparts distinctive depth profiles in $\delta^{37}Cl$ values, with δ values decreasing in the opposite direction of advective water flow. In comparison, the authors found that in well-drained soils of warm deserts, brine movement is downward due to rare rainfalls, which appear to cause small fractionations from Rayleigh-like processes. There, the dissolution and reprecipitation of NaCl is identifiable as a consistent decrease in $\delta^{37}Cl$ values with depth (as described above in Section 4.5.2). The isotope fractionation factor between NaCl and a saturated solution is 0.26 ± 0.7‰ at 22 ± 2 °C (Eggenkamp et al., 1995). Halite formed from seawater (0.00‰) via equilibrium fractionation is reported to have values ranging from −0.6 to +0.4‰ due to multiple precipitation and dissolution events. Values >0.4‰ cannot arise from evaporation of seawater and imply an alternative mechanism of formation, such as influx of a non-zero ‰ fluid (Eastoe and Peryt, 1999). The $\delta^{37}Cl$ values of chlorine in the Qh site ranged from −1.4 to 0.3‰, and from −0.6 to 0.8‰ in the Qp soil. The groundwater from the Qh site has a value of 0.19‰ (Fig. 10; Table 5). The weighted average of the chlorine is −0.2‰ and 0.0‰ at the Qh and Qp sites, respectively.

Over 90% of the soil chlorine is in the cemented halite layers on the surface of the soils: 22 cm thickness at Qh and 51 cm thickness at Qp (Fig. 8; Table 2). Given what we know about these sites, key processes that may impact chlorine distribution and isotopic composition include:

1. Long-term net migration of NaCl upwards via capillary rise and evaporation of groundwater. This would be an advective process and should result in little isotopic fractionation.
2. Downward diffusion of chlorine in response to concentration gradients induced by evaporation and deposition of salts higher in the soil profile. Due to differences in diffusivities among isotopologues, this would cause a decrease in $\delta^{37}Cl$ with depth because ^{35}Cl diffuses more quickly than ^{37}Cl (Desaulniers et al., 1986).
3. Inputs to the crust from aeolian redistribution of Miocene halite and from sea salt deposition. Given the isotopic similarity between the two sources, it may not be possible to isotopically differentiate these.

Repeated dissolution and reprecipitation of the crust driven by deliquescence and efflorescence associated with fog events (Section 4.6). This may cause small spatial scale variations in chlorine isotope ratios. However, detecting this would require precise sampling along presumed growth features, which we did not attempt.

4. Ion filtration in which a negatively charged membrane (e.g., a clay layer) repels Cl^- in an advective flow regime. Because ^{35}Cl has a higher ionic mobility than ^{37}Cl, it tends to become enriched behind the membrane relative to the direction of flow (Phillips and Bentley, 1987). This is likely not a factor for these soils as no significant "membrane" layer is present, and regions of higher Cl concentration are not associated with lower $\delta^{37}Cl$, as would be expected if ion filtration were occurring.

Below ~20 cm, $\delta^{37}Cl$ values decrease 1.3‰ with depth at both sites. Among the five processes listed above, the isotope fractionating process we anticipate to be operable is #2, which should cause a decrease in $\delta^{37}Cl$ values with increasing depth as a result of chlorine diffusion along concentration gradients in pore water.

In the upper ~10 cm, the $\delta^{37}Cl$ values are nearly identical at -0.30 ± 0.13‰ ($n = 3$) and -0.24 ± 0.08‰ ($n = 2$) at the Qh and Qp sites, respectively. For comparison, two samples from the Salar de Atacama averaged -0.21 ± 0.11‰ ($n = 4$) and -0.13 ± 0.12‰ ($n = 3$), and one sample from the Salar Grande averaged -0.28 ± 0.14‰ ($n = 2$) (Amundson et al., 2012). Given the similarity in all of these values, we hypothesize that the surface crusts receive inputs from both sea salt and recycled Andean material, and become relatively homogenized due to fog water and (very rare) rainwater (processes #3 and #4 above). Below this homogenized and "active" zone, the declining $\delta^{37}Cl$ values with depth are consistent with process #2 above.

Although chlorine isotope research in hyperarid soils is only in its infancy, and the fractionation seen here is modest, the data provide support for two important processes impacting the halite accumulation in salars: (1) dynamic and semi-continuous alteration of the surficial "active" zone of the crusts and (2) a net downward ionic diffusion and isotope fractionation along chlorine concentration gradients.

4.5.4. Carbonate stable isotope ratios

Well-drained soils in the hyperarid Atacama Desert contain little or no carbonate due to a combination of high sulfate concentrations and low soil pCO_2 levels (Ewing et al., 2006; Quade et al., 2007). In these salar soils, carbonate is present in varying amounts at different depths and between the sites (Fig. 8; Table 2). Since the soils contain little organic matter, we use total %C as a proxy for $\%CO_3$. At site Qp, the %C is fairly constant throughout the profile, ranging from 0.25% to 0.76%. However, at the Qh site the %C is more variable, increasing from 0.04% at the surface to >2% deeper in the profile. The carbonate in these soils is likely derived both from sediment deposition (e.g., fresh water marls), and from pedogenic processes after the drying of the lakes/wetlands. In particular, the large and irregular concentrations of carbonate within the Qh soil are presumed to largely reflect pre-soil forming processes that occurred within the lacustrine/wetland environment. Therefore, much of the carbonate between 37 and 94 cm in the Qh soil is likely lacustrine in origin, unlike the carbonate at the Qp site which may reflect pedogenic processes that occurred after lake drying. This is important when considering the stable isotope composition of the carbonate at the two sites.

When pedogenic carbonates form they incorporate carbon from soil CO_2, which is a mix from both biological and atmospheric sources. The $\delta^{13}C$ value of carbonates therefore can be used to determine the proportion of each source present at the time of formation (Cerling and Quade, 1993). Quade et al. (2007) showed that carbonates that form in the near absence of biological activity have $\delta^{13}C$ values of +4‰, whereas carbonates formed under the influence of plants and microbial processes can attain values as low as −14‰ (Cerling and Quade, 1993).

In the Qh profile, the $\delta^{13}C$ value of carbonate in the surface horizon is −5.29‰, and increases steadily with depth to ~0‰ at 37 cm. Values remain constant to 94 cm, and then quickly decline to −5‰ at the base of the soil (Fig. 11; Table 5). There is a very low concentration of carbonate in the surficial halite crust. The surprisingly negative $\delta^{13}C$ values can be attributed to the in situ biological activity of the microbial communities living there, and the associated small amount of carbonate forming in the vicinity of this biological respiration. The remaining carbonate in the Qh profile likely is a variable mix of sedimentary and pedogenically formed minerals.

The $\delta^{13}C$ values of carbonate in the Qp profile average −3.1‰ and vary little with depth. Assuming that the carbon isotopes are derived from diffusing soil CO_2, this reflects steady state $\delta^{13}C$ values of about −17.5‰. The lack of a depth trend in C isotopes may reflect the dense halite cap on the soil, facilitating a very sharp transition between the soil and overlying atmospheric CO_2.

Further insight into the carbonate forming environments can be gained from the $\delta^{18}O$ values. While the $\delta^{13}C$ value of pedogenic carbonate reflects the soil CO_2 at the time of formation, the $\delta^{18}O$ values of the carbonates reflects the $\delta^{18}O$ value of the soil water. Aravena et al. (1989) determined that the $\delta^{18}O$ values of groundwater in the region range from −5.9 to −4‰ and fog water ranges from −2.7 to −1‰. The groundwater largely reflects runoff and subsurface flow derived from rainfall at higher elevations to the east. At both of the Qh and Qp sites, the carbonates at the surface have $\delta^{18}O$ values of ~24‰ SMOW (Fig. 11; Table 5). After accounting for the fractionation between liquid water and carbonates (29.1‰ at 20 °C; Kim and O'Neil (1997)), the surface carbonate values reflect water sources that have $\delta^{18}O$ values of −4.26‰ and −5.2‰ at the Qh and Qp sites, respectively.

At the Qp site, the $\delta^{18}O$ value is fairly constant and does not change significantly with depth. In contrast, at the Qh site the $\delta^{18}O$ value decreases slightly to +21.6‰ in the layer below the surface, then sharply increases to +34.3‰ at 37 cm. The values remain constant until the base of the soil when they decrease to ~27.8‰. At the Qh site, the $\delta^{13}C$ and $\delta^{18}O$ isotope trends mirror each other with depth. The $\delta^{13}C$ and $\delta^{18}O$ values increase with depth, and the high concentrations of carbonate between ~20–100 cm are interpreted as reflecting lacustrine origins (Table 2). The very positive $\delta^{18}O$ values reflect formation waters of about ~6‰, which would require considerable evaporation from the present groundwater values. Consistent with this interpretation, the $\delta^{13}C$ values indicate a CO_2 source of ~−9 to −10‰, which indicates a low percentage of biologically processed CO_2. In general, for the Qh soil, we interpret the upper three layers have experienced varying degrees of alteration or pedogenic carbonate formation – with the surface layer especially reflecting in situ isotopic signatures derived from the biotic-rich halite crust. The carbonate-rich layers from ~40–90 cm, due to the high carbonate concentrations and the highly enriched $\delta^{13}C$ and $\delta^{18}O$ values, appear to reflect formation in a highly evaporated lake setting. The $\delta^{18}O$ values in Qp are all consistent with un-

evaporated groundwater, and the $\delta^{13}C$ values reflect a CO_2 source of about −12 to −13‰.

4.5.5. Trace metal concentrations

Both the Qh and Qp soils have high levels of arsenic, selenium, and molybdenum, with ranges of 21–250 ppm, 0.4–3.4 ppm, and 2–96 ppm, respectively (Table 2). Arsenic is depth invariant in both soils, but found at concentrations 3× greater in the Qh soil than in the Qp soil. Selenium and molybdenum have pronounced increases in concentration near the surface in both soils (within the halite (Bzm) horizons). Selenium concentrations are similar between the two sites, and molybdenum is similar in low levels between the sites, but 6× greater at the surface of Qh than the Qp soil. High concentrations of these metals/metalloids in the regional groundwater and surface water are well documented and linked to volcanic activity (Bhattacharya et al., 2002; Leybourne and Cameron, 2008; Demergasso et al., 2007; Romero et al., 2003). Cameron and Leybourne (2005) studied soils in the northern Atacama Desert and similarly found high levels of arsenic, selenium, and molybdenum and concluded that they are dissolved as anions in the groundwater and are evapo-concentrated in the soils. This process has been known to occur in agricultural evaporation ponds in the San Joaquin Valley of California (Ong et al., 1997). We recognize that wind-borne dust may supply some of these metals, however given the water concentrations, it seems that evaporation of groundwater is the main driver of the observed trends. Differences in concentrations between the sites are likely due to differences in groundwater concentrations or length of chemical evolution path (depth to groundwater).

4.6. Dynamics of salt crust modification and microbial activity

One of the most distinctive features of the salt encrusted landscape of the Atacama Desert is its rugged, and nearly impenetrable, physical nature. Artieda et al. (2015) described the crust morphology and inferred the development pattern of four salars in the Atacama Desert, ranging from salars which receive ample fog and whose crusts are therefore frequently able to deliquesce, to those which do not receive regular fog and do not deliquesce often. One of their "wet" end members was the Salar Llamara, which is described here. Here, we add to this previous work with an in-depth examination of the climatic conditions, both inside and outside the salt crusts, and an assessment of the environment's ability to support microbial life within the crusts.

The crusts in our field areas display desiccation polygons surrounded by halite nodules jutting up from the ground along the polygon cracks (Fig. 12). Though these surfaces are largely sealed, we have shown earlier that the cracks and fissures in the crusts allow upward movement of groundwater. Surface nodules are capable of deliquescing when the relative humidity exceeds 75%, further shaping the hydrology and physical nature of the crusts (Davila et al., 2008). To better understand the frequency of these processes, we examine micrometeorological observations of these landscapes.

4.6.1. Site meteorological conditions

At the Qp site 14 months of meteorological data were recorded, but at the Qh site the weather station stopped recording temperature and relative humidity after three months. During the three-month period with overlapping data, both the Qh and the Qp sites had very similar temperature and relative humidity diurnal cycles. Temperature often varied from 0 to 30 °C over a 24 h period, with the maximum between 1:00–3:00 pm and minimum between 5:30–8:30 am. Relative humidity often fluctuated between 10 and 90%, peaking in the early mornings between 1:00–8:30 am, and reaching minimum values between 1:00–3:00 pm (Fig. 13).

The temperature at the two sites does not appear to be significantly different, but there were small differences in the relative humidity. The median relative humidity at the Qh site is 61%, whereas the median relative humidity at the Qp site is 56%. The leaf wetness sensors support the finding that the Qp site is less humid than the Qh on average. It appears from our data that the presence of moisture on the leaf wetness sensors roughly correlates with sustained atmospheric relative humidity ≥75% at temperature's ranging from 0 to 7 °C. Over the entire year of observation, the Qh leaf wetness sensor measured 1567 h of moisture and the Qp leaf wetness sensor measured 901 h of moisture (out of a possible 9504 h).

4.6.2. Microclimate conditions within the crusts

Previous work has shown that microbial communities are capable of colonizing halite crusts due to liquid water made available during deliquescence (Davila et al., 2013, 2008; Wierzchos et al., 2012). As the relative humidity reaches and exceeds 75%, halite within the salt crusts converts to a liquid brine solution. The sensors installed in the crusts at our sites reveal the duration and temporal patterns of deliquescence. A detailed discussion of the atmospheric conditions can be found in the above Section 4.6.1.

Here we focus on the conditions within the crusts, derived from seven temperature and relative humidity sensors at each site (Fig. 5). Temperature within the crusts at both sites varies on a diurnal cycle from ~0 to 40 °C, and there is no significant difference between temperatures at the two sites. The sensors also reveal that the internal crust environment has a relative humidity ≥75% for most of the study period (14 months). On average, the sensors at the Qh site were below 75% relative humidity 19% of the time, while the Qp sensors were below 75% relative humidity only 3% of the time. Fig. 13 illustrates in detail a typical week within the crust during July 2013. Even when the atmospheric relative humidity drops well below 75% the crusts are able to maintain an internal relative humidity ≥75%. Wierzchos et al. (2012) similarly found this to be true at their study site, and noted that once a nodule reaches a relative humidity >75%, it is able to maintain this condition for prolonged periods of time regardless of the external relative humidity.

Table 6 provides the details of how long each individual sensor was below 75%, and which season this threshold in relative humidity occurred. Summer months (Dec–Feb) experienced the most intensive drying at both sites. At the Qh site, fall (Mar–May) and spring (Sep–Nov) experienced similar drops in crust relative humidity, while at the Qp site spring (Sep–Nov) was much drier than fall (Mar–May). The differences between the sites may be due to differences in site metrological conditions (as recorded by the leaf wetness sensors) or to differences in installation techniques. As discussed in Section 3.2, sensors at the Qp site were installed in nodules that were first sectioned using an electric hand saw, while the sensors at the Qh site were installed directly into whole nodules (Fig. 5). We are unable to definitively determine if this had any effect on the results, though we note that the sensors at the Qp site were placed within a much denser salt mass than at the Qh site.

Davila et al. (2008) conducted a similar experiment at the Yungay field station located at higher elevations and further inland. In general, fog and the intrusion of marine air is less pronounced there due to its geographical location. They found that the relative humidity within the halite crusts at Yungay were >75% for only 214 h during the study year and reported an average atmospheric relative humidity of 37%. Another study in the region by Wierzchos et al. (2012) reported relative humidity >75% within halite nodules for 3909 h over the year.

We conclude that the nodules at the Qh and Qp sites are able to strongly buffer diurnal changes in atmospheric relative humidity and almost never fully dry out, unlike some nodules further inland. At our sites in the Salar Llamara, likely only the very outer layers of the nodules undergo daily cycles of deliquescence and efflorescence, though due to the size of our sensors, we were unable to capture these conditions.

4.6.3. Rates of biological activity and crust formation

The halite crusts contain prominent green pigments from microbial communities (Fig. 14). To gain an understanding of the rate of carbon turnover in these crusts, organic carbon from three halite nodules on the surface at each site was dated. All of the samples from the Qh site

Table 6
Average temperature and relative humidity within the halite nodules. Seven Onset HOBO® Pro v2 (U23-002) sensors were installed at each site. The number of hours recorded with RH < 75% was calculated and are presented as a percent of hours recorded (9504 total). The timing of these RH < 75% events is given by season as percent of the total RH < 75% events. Installation techniques were slightly different at each site (Fig. 2), allowing for measurement deeper within the nodules at the Qp site.

	Max T (°C)	Avg T (°C)	Min T (°C)	Max RH (%)	Avg RH (%)	Min RH (%)	Hours RH < 75%	Timing of RH < 75% events (as a % of all events)			
Sensor	All year						%	Dec–Feb	Mar–May	Jun–Aug	Sep–Nov
Qh 1	48	19	−5	83	77	14	17	36	19	24	20
Qh 2	50	19	−6	79	74	60	33	44	44	2	10
Qh 3	50	19	−6	84	79	35	1	100	0	0	0
Qh 4	48	18	−4	82	76	17	22	46	20	20	15
Qh 5	48	19	−5	81	77	25	15	53	13	22	12
Qh 6	49	19	−6	84	78	21	7	38	16	32	15
Qh 7	48	18	−5	80	74	18	37	45	25	12	19
Qp 1	48	19	−4	82	79	21	2	90	5	0	4
Qp 2	47	19	−4	81	77	20	8	68	23	1	8
Qp 3	49	19	−3	87	80	56	3	72	0	16	11
Qp 4	48	19	−4	86	80	75	0	0	0	0	0
Qp 5	49	19	−5	84	79	21	4	61	0	2	37
Qp 6	48	19	−4	82	79	26	3	72	0	0	28
Qp 7	48	19	−4	82	79	21	3	74	6	0	20

are radiocarbon "modern", indicating the accumulation of organic carbon in the past few decades, and active photosynthesis and organic carbon cycling. However, at the Qp site, the radiocarbon ages of occluded organic carbon are 2546, 8521, and 1995 cal yr BP (Table 1). This indicates not only that microbial communities appear far less active here with a much slower carbon cycling rate, but also that these nodules (or at least the organic carbon within them) have been on the surface of this playa for well over 2000 years. Though this suggests that at least portions of these salt crusts are highly stable features, there is also ample evidence that shows that some portions of the crusts are physically dynamic and subject to alteration. Wind and water both sculpt and modify the crusts, while evaporation of groundwater likely continues – at least at the Qh site with a thinner crust – to add salt at the crust base and heave the overlying material upward.

4.6.4. Proposed conceptual model of salt crust formation

From our observations we propose the following conceptual model for salt crust formation in this salar. First, lake desiccation due to climate change and/or tectonics leads to the lowering of the water table. Capillary rise from evaporation of shallow groundwater leads to the deposition of salts on the surface of the soil. A solid layer of salt crust eventually forms, and is pushed up and physically modified as salts continue to accumulate. Evaporative stress and thermal drying create cracking polygons, and salts begin to accumulate faster in the regions around the polygon edges. Salts continue to increase and form protrusions around the polygons. These nodules evolve geomorphically as wind and water sculpt them. Simultaneously, atmospheric relative humidity rises beyond a threshold relative humidity for deliquescence within the nodules. This deliquescence provides liquid water for microbial communities. After reaching a large enough size, the internal environment of the nodules are able to buffer diurnal changes in atmospheric relative humidity, allowing for a sustained habitable microenvironment.

5. Conclusions

Evaporation of shallow groundwater in salars of the Atacama Desert drives the geochemical evolution of these soils, currently classified as Gypsic Haplosalids. In a previous paper, we suggest taxonomic changes that would classify the soils as Epi Petrosalids, emphasizing both the indurated surface and the relative direction of fluid and surface salt accumulation (Finstad et al., 2014). Rates of evaporation were found to average ~ 0.03 mm m^{-2} d^{-1} over geologic time at both sites. This continuous process leads to the accumulation and growth of salt crusts on the soil surface, which in turn decreases the rate of groundwater evaporation. Rates of evaporation from an experimental plot at the Qh site, where the salt crust was largely removed, were observed to be 38× faster than the calculated geologic rate. This upward movement of water and its dissolved solutes produces a salt profile with the most soluble salts on the surface and the least soluble at the base, as salts are deposited as their solubility coefficients are exceeded. This is the opposite trajectory observed in other desert soils and well-drained soils in the Atacama Desert. However, evaporitic environments exist in arid regions around the world, and the processes examined here may be applicable to locales such as in the Mojave Desert in California, the Western Desert in Egypt, and the Arabian Desert in Saudi Arabia.

Stable isotope ratios of sulfate, chloride, and carbonate were used to infer geochemical processes occurring within the soils. The $\delta^{34}S$ values of sulfate provided depth patterns that were consistent with the upward water movement and associated Rayleigh-like fractionation associated with repeated mineral dissolution and precipitation. This process tends to leave heavier sulfur isotopes deeper in the soil and lighter sulfur isotopes are preferentially transported toward the surface of the soil profiles. $\delta^{37}Cl$ values of soil water indicated that the surface crusts are dynamic, and provided evidence for downward ionic diffusion that counters the upward advective movement of water and solutes. $\delta^{13}C$ and $\delta^{18}O$ values of carbonate suggest that the uppermost halite layers contain surprisingly small amounts of carbonate with a strong biological isotope signature, reflecting the effects of microbial communities within the deliquescing halite. The carbonate-rich marl from ~40–90 cm in the Qh soil provide evidence for evaporitic lake conditions. The ages of the two salars, which both required significant water to form, correspond well with the now well established CAPE pluvial episodes that left evidence throughout the region. However, until now, the impact of these events on basin deposits in the desert had not been fully recognized.

This unique pedogenic setting is still actively undergoing soil development. Unlike other playas that undergo cycles of wetting and drying, the Salar Llamara has experienced near continuous evaporation since the final stages of lake/marsh drying, resulting in the very unique salt crusts on the land surface. Evaporation appears to continue to add salt, and any physical modification of the land surface results in a rapid redevelopment of crusts by increased rates of evaporation. Despite no recorded rainfall, the internal surface crust environment maintains a nearly steady relative humidity at or above deliquesce relative humidity (75%) the majority of the 14-month period of observation. We conclude that these crusts are able to buffer diurnal changes in atmospheric relative humidity and almost never fully dry out, unlike nodules further inland. This maintenance of liquid water results in active microbial communities, and radiocarbon measurements indicate that carbon cycling is occurring at decadal time scales.

Acknowledgements

We are grateful for all the support received while completing this work. Funding to K.F. through the NASA Earth and Space Sciences Fellowship and NSF Doctoral Dissertation Improvement Grant, to M.P. through the CONICYT for Becas Chile Scholarship and the Fulbright Foreign Student Program Scholarship, and to R.A. through the University of California Agricultural Experiment Station and NSF grant # 0819972. We would like to thank D. Drew for help with chlorine isotope analyses. Finally, we thank the reviewers for their thoughtful and thorough comments which have strengthened this manuscript.

References

Allmendinger, R.W., González, G., Yu, J., Hoke, G., Isacks, B., 2005. Trench-parallel shortening in the Northern Chilean Forearc: tectonic and climatic implications. America Bulletin.]–>Geol. Soc. Am. Bull. 117, 89.

Amundson, R., Barnes, J., Ewing, S.A., Heimsath, A.M., Chong, G., 2012. The stable isotope composition of halite and sulfate of hyperarid soils and its relation to aqueous transport. Geochim. Cosmochim. Acta 99, 271–286.

Aravena, R., Suzuki, O., Pollastri, A., 1989. Coastal fog and its relation to groundwater in the IV region of northern Chile. Chem. Geol. 79, 83–91.

Artieda, O., Davila, A.F., Wierzchos, J., Buhler, P., Rodríguez-Ochoa, R., Pueyo, J., Ascaso, C., 2015. Surface evolution of salt-encrusted playas under extreme and continued dryness. Earth Surf. Process. Landf. 40, 1939–1950.

Bao, H., Campbell, D.A., Bockheim, J.G., Thiemens, M., 2000. Origins of Sulphate in Antarctic Dry-Valley soils as deduced from anomalous ^{17}O compositions. Nature 407, 499–502.

Barnes, J., Sharp, Z.D., 2006. A chlorine isotope study of DSDP/ODP serpentinized ultramafic rocks: insights into the Serpentinization process. Chem. Geol. 228, 246–265.

Bhattacharya, P., Frisbie, S.H., Smith, E., Naidu, R., Jacks, G., Sarkar, B., 2002. Arsenic in the environment: a global perspective. In: Sarkar, B. (Ed.), Handbook of Heavy Metals in the Environment. Marcell Dekker Inc, New York, pp. 147–215.

Bittelli, M., Ventura, F., Campbell, G.S., Snyder, R.L., Gallegati, F., Pisa, P.R., 2008. Coupling of heat, water vapor, and liquid water fluxes to compute evaporation in bare soils. J. Hydrol. 362, 191–205.

Boschetti, T., Cortecci, G., Barbieri, M., Mussi, M., 2007. New and past geochemical data on fresh to brine waters of the Salar de Atacama and Andean Altiplano, northern Chile. Geofluids 7, 33–50.

Cameron, E.M., Leybourne, M., 2005. Relationship between groundwater chemistry and soil geochemical anomalies at the Spence copper porphyry deposit, Chile. Geochem. Explor. Environ. Anal. 5, 135–145.

Cerling, T., Quade, J., 1993. Stable carbon and oxygen isotopes in soil carbonates. In: Swart, P.K., Lohmann, K.C., McKenzie, J., Savin, S. (Eds.), Climate Change in Continental Isotope Records. American Geophysical Union, Washington, DC, pp. 217–231.

Chong, G., 1984. Die salare in Nordchile — geologie struktur und geochemie. Geotekton. Forsch. 67, 1–146.

Chong, G., Pueyo, J., Demergasso, C., 2000. The borate deposits in Chile. Chile.]–>Rev. Geol. Chile 27, 99–119.

Criss, R.E., 1999. Principles of Stable Isotope Distribution. Oxford University Press, pp. 1–254.

Davila, A.F., Gómez-Silva, B., de los Rios, A., Ascaso, C., Olivares, H., McKay, C.P., Wierzchos, J., 2008. Facilitation of endolithic microbial survival in the hyperarid core of the Atacama Desert by mineral deliquescence. J. Geophys. Res. 113, 1–9.

Davila, A.F., Hawes, I., Ascaso, C., Wierzchos, J., 2013. Salt deliquescence drives photosynthesis in the hyperarid Atacama Desert. Environ. Microbiol. Rep. 5, 583–587.

Demergasso, C.S., Guillermo, C.D., Lorena, E.G., Mur, J.J.P., Pedros-Alio, C., 2007. Microbial precipitation of arsenic sulfides in Andean salt flats. Geomicrobiol J. 24, 111–123.

Desaulniers, D.E., Kaufmann, R.S., Cherry, J.A., 1986. ^{37}Cl-^{35}Cl variations in a diffusion controlled groundwater system. Geochim. Cosmochim. Acta 50, 1757–1764.

Eastoe, C.J., Peryt, T.M., 1999. Stable chlorine isotope evidence for non-marine chloride in Badenian evaporites. Carpathian Mountain Region. Terra Nova. 118–123.

Eggenkamp, H.G.M., 1994. The Geochemistry of Chlorine Isotopes. Ph.D. Thesis. Universiteit Utrecht, pp. 1–151.

Eggenkamp, H.G.M., Kreulen, R., Koster Van Groos, A.F., 1995. Chlorine stable isotope fractionation in evaporites. Geochim. Cosmochim. Acta 59, 5169–5175.

Ericksen, G.E., Salas, R.O., 1990. Geology and resources of Salars in the Central Andes. In: Ericksen, G.E., Canas Pinochet, M.T., Reinemund, J.A. (Eds.), Geology of the Andes and Its Relation to Hydrocarbon and Mineral Resources. Circum-Pacific Council for Energy and Mineral Resources, Houston, Texas, pp. 151–164.

Ewing, S.A., Sutter, B., Owen, J., Nishiizumi, K., Sharp, W., Cliff, S.S., Perry, K., Dietrich, W., McKay, C.P., Amundson, R., 2006. A threshold in soil formation at Earth's arid–hyperarid transition. Geochim. Cosmochim. Acta 70, 5293–5322.

Ewing, S.A., Yang, W., DePaolo, D.J., Michalski, G., Kendall, C., Stewart, B.W., Thiemens, M., Amundson, R., 2008. Non-biological fractionation of stable Ca isotopes in soils of the Atacama Desert. Chile. Geochimica et Cosmochimica Acta. 72, 1096–1110.

Finstad, K., Pfeiffer, M., Amundson, R., 2014. Hyperarid soils and the soil taxonomy. America Journal.]–>Soil Sci. Soc. Am. J. 78, 1845–1851.

Gayo, E.M., Latorre, C., Jordan, T.E., Nester, P.L., Estay, S.A., Ojeda, K.F., Santoro, C.M., 2012. Late quaternary hydrological and ecological changes in the hyperarid core of the northern Atacama Desert (~21°S). Earth Sci. Rev. 113, 120–140.

Hogg, A., Hua, Q., Blackwell, P., Niu, M., Buck, C., Guilderson, T., Heaton, T., Palmer, J., Reimer, P., Reimer, R., Turney, C., Zimmerman, S., 2013. SHCAL13 southern hemisphere calibration, 0–50,000 years cal bp. Radiocarbon 55, 1889–1903.

Houston, J., 2006. Evaporation in the Atacama Desert: an empirical study of spatio-temporal variations and their causes. J. Hydrol. 330, 402–412.

Hua, Q., Barbetti, M., Rakowski, A., 2013. Atmospheric radiocarbon for the period 1950–2010. Radiocarbon 55, 2059–2072.

Jordan, T.E., Kirk-Lawlor, N.E., Blanco, N.P., Rech, J.A., Cosentino, N.J., 2014. Landscape modification in response to repeated onset of hyperarid paleoclimate states since 14 Ma, Atacama Desert, Chile. Geol. Soc. Am. Bull. 126, 1016–1046.

Kampf, S.K., Tyler, S.W., Ortiz, C.A., Muñoz, J.F., Adkins, P.L., 2005. Evaporation and land surface energy budget at the Salar de Atacama, Northern Chile. J. Hydrol. 310, 236–252.

Kim, S.T., O'Neil, J.R., 1997. Equilibrium and nonequilibrium oxygen isotope effects in synthetic carbonates. Geochim. Cosmochim. Acta 61, 3461–3475.

Latorre, C., Santoro, C.M., Ugalde, P.C., Gayo, E.M., Osorio, D., Salas-Egaña, C., De Pol-Holz, R., Joly, D., Rech, J.A., 2013. Late Pleistocene human occupation of the hyperarid core in the Atacama Desert, northern Chile. Quat. Sci. Rev. 77, 19–30.

Leybourne, M.I., Cameron, E.M., 2008. Source, transport, and fate of rhenium, selenium, molybdenum, arsenic, and copper in groundwater associated with porphyry–Cu deposits, Atacama Desert. Chile. Chemical Geology. 247, 208–228.

Lowenstein, T.K., Hardie, L., 1985. Criteria for the recognition of salt-pan evaporites. Sedimentology 32, 627–644.

Magaritz, M., Aravena, R., Peña, H., Suzuki, O., Grilli, A., 1989. Water chemistry and isotope study of streams and springs in northern Chile. J. Hydrol. 108, 323–341.

Michalski, G., Bohlke, J.K., Thiemens, M., 2004. Long term atmospheric deposition as the source of nitrate and other salts in the Atacama Desert. Chile: New evidence from mass-independent oxygen isotopic compositions. Geochimica et Cosmochimica Acta. 68, 4023–4038.

Nester, P.L., Gayo, E.M., Latorre, C., Jordan, T.E., Blanco, N., 2007. Perennial stream discharge in the hyperarid Atacama Desert of northern Chile during the latest Pleistocene. Proc. Natl. Acad. Sci. 104, 19724–19729.

Ong, C., Herbel, M., Dahlgren, R., Tanji, K., 1997. Trace element (Se, As, Mo, B) contamination of evaporites in Hypersaline agricultural evaporation ponds. Environ. Sci. Technol. 31, 831–836.

Perez-Fodich, A., Reich, M., Alvarez, F., Snyder, G.T., Schoenberg, R., Vargas, G., Muramatsu, Y., Fehn, U., 2014. Climate change and tectonic uplift triggered the formation of the Atacama Desert's giant nitrate deposits. Geology 42, 251–254.

Phillips, F.M., Bentley, H.W., 1987. Isotopic fractionation during ion filtration: I. Theory. Geochim. Cosmochim. Acta. 51, 683–695.

Pueyo, J.J., Chong, G., Jensen, A., 2001. Neogene evaporites in desert volcanic environments: Atacama Desert, northern Chile. Sedimentology 48, 1411–1431.

Quade, J., Rech, J.A., Latorre, C., Betancourt, J.L., Gleeson, E., Kalin, M.T.K., 2007. Soils at the hyperarid margin: the isotopic composition of soil carebonate from the Atacama Desert, Northern Chile. Geochim. Cosmochim. Acta 71, 3772–3795.

Quade, J., Rech, J.A., Betancourt, J.L., Latorre, C., Quade, B., Rylander, K.A., Fisher, T., 2008. Paleowetlands and regional climate change in the central Atacama Desert, northern Chile. Quat. Res. 69, 343–360.

Quezada, A., Vasquez, P., Sepulveda, F., White, N., Tomlinson, A., 2012. Mapa compilación geológica área Quillagua-Salar Grande Región de Tarapacá.

Rech, J.A., Quade, J., Betancourt, J.L., 2002. Late quaternary paleohydrology of the central Atacama Desert (lat 22–24 S). Chile. GSA Bulletin. 114, 334–348.

Rech, J.A., Quade, J., Hart, W.S., 2003. Isotopic evidence for the source of Ca and S in soil gypsum, anhydrite and calcite in the Atacama Desert, Chile. Geochim. Cosmochim. Acta 67, 575–586.

Romero, L., Alonso, H., Campano, P., Fanfani, L., Cidu, R., Dadea, C., Keegan, T., Thornton, I., Farago, M., 2003. Arsenic enrichment in waters and sediments of the Rio Loa (Second Region, Chile). Appl. Geochem. 18, 1399–1416.

Saez, A., Cabrera, L., Chong, G., 1999. Late Neogene lacustrine record and palaeogeography in the Quillagua–Llamara basin, Central Andean fore-arc (northern Chile). Palaeogeogr. Palaeoclimatol. Palaeoecol. 151, 5–37.

Sharp, Z.D., Barnes, J., Brearley, A.J., Chaussidon, M., Fischer, T.P., Kamenetsky, V.S., 2007. Chlorine isotope homogeneity of the mantle, crust and carbonaceous chondrites. Nature 446, 1062–1065.

Soil Survey Staff, 1999. Soil Taxonomy: A Basic System of Soil Classification for Making and Interpreting Soil Surveys. 2nd edition. Natural Resources Conservation Service. 436. US Department of Agriculture Handbook.

Stoertz, G.E., Ericksen, G.E., 1974. Geology of Salars in Northern Chile. Geological Survey Professional Paper 811.

Stuiver, M., Polach, H., 1977. Reporting of 14C data. Radiocarbon 19, 355–363.

Thode, H.G., Monster, J., 1965. Sulfur isotope geochemistry of petroleum. Evaporites, and Ancient Seas, American Association of Petroleum Geologists, Memorial 4, 367–377.

Vogel, J.S., Southon, J.R., Nelson, D.E., Brown, T.A., 1984. Performance of catalytically condensed carbon for use in accelerator mass spectrometry. Nuclear Instruments and Methods in Physics Research. B5, 289–293.

Weisbrod, N., Dragila, M.I., 2006. Potential impact of convective fracture venting on salt-crust buildup and ground-water salinization in arid environments. J. Arid Environ. 65, 386–399.

Wierzchos, J., Davila, A.F., Sánchez-Almazo, I.M., Hajnos, M., Swieboda, R., Ascaso, C., 2012. Novel water source for endolithic life in the hyperarid core of the Atacama Desert. Biogeosciences 9, 2275–2286.